PALACKÝ UNIVERSITY

FACULTY OF NATURAL SCIENCES

Department of Optics

Generation of Correlated Photons With Time Resolution

Lukáš Slodička

Olomouc 2008

Abstract

In the presented experimental thesis the three-photon source based on the spontaneous parametric down-conversion and attenuated coherent beam has been realized. The fundamental pulses obtained from femtosecond laser are used for pumping the nonlinear process of second harmonic generation. The depleted fundamental beam is attenuated to single photon level, while the generated frequency doubled UV beam is spatially filtered and used for pumping the process of spontaneous parametric down-conversion. The spatial filtering of the high power UV beam by the single-mode step-index as well as photonic fibers and by 4-f system has been extensively studied including the spectrum broadening by self-phase modulation in both mentioned fiber types. Two-photon Hong-Ou-Mandel interference with almost unity visibility has been achieved between photons from generated pair. The high visibility of three-photon Rarity-Tapster interference between the weak coherent beam and triggered single-photon state from the down-converted pair together with the sufficient rate of the threefold coincidence events confirms the suitability of the source for experiments in the field of quantum information processing.

Acknowledgments

Most of all, I would like to thank my supervisor and colleague Miroslav Ježek for his continuous and generous support and professional help with solving both the experimental and the theoretical problems. His help has been invaluable for me.

Big thanks are also due to other members of Department of Optics and Joint Laboratory of Optics of Palacký University and AS CR, especially Doc. Jaromír Fiurášek Ph.D., Doc. RNDr. Ondřej Haderka, Ph.D., and Mgr. Jan Soubusta, Ph.D. for valuable discussions and technical support.

I am very grateful to my loving parents Peter and Helena and brother Peter for their love and care, and especially for always being there for me.

<div align="right">LUKÁŠ SLODIČKA</div>

Contents

Chapter 1

Introduction

Quantum mechanics changed our common understanding of physical world. Since the time of Max Planck discover that the energy could only be a multiple of an elementary unit more than hundred years ago the field of quantum mechanics expanded into immense subject area. Its principles and results are nowadays used in any natural and technical science research. The basic principles of the quantum world are the non-locality and superposition principle. Quantum superposition principle enables to describe the quantum bits and the non-locality allow to think about correlations and entanglement between distant particles and systems. Both the principles give rise to new class of classically unacceptable phenomena. Non-locality together with superposition principle enabled the birth of unique field of quantum information processing which cover the quantum computation and communication.

Field of quantum information processing has achieved considerable accomplishments in last decade, but many challenging tasks remain still unresolved. There are plenty of theoretical proposals engaging in the quantum computing, the most famous are perhaps Shor's factorization algorithm [1] and Grover's search algorithm [2]. Although both algorithms have been successfully realized using photonic q-bits [3] or atomic ensembles [4, 5], experiments were only proof of principle demonstrations of the proposed algorithms, not the practically usable devices. The same situation is in the field of quantum communication where proposals for complete communication system between two distant parties include quantum cryptography, teleportation, entanglement swapping, and purification. All parts of such communication system have been already successfully realized [6, 7, 8], however, there are arising several fundamental problems in the realization of the complex scheme. They can be divided into three subgroups. Generation of the quantum ensemble suitable for information protocol, decoherence during the run of the experiment, and inefficiencies associated with detection. Therefore, much of the nowadays effort in experimental quantum information is directed toward the realization of the source of suitable quantum ensemble on which information can be encoded, properly manipulated, and read.

Suitable candidates for quantum bits for realizations of quantum information protocols

are photons. Photons are robust against decoherence since they do not interact with environment and they can be easily manipulated. The major challenge is the generation of photon-number states. Various approaches to generation of such states have been proposed and implemented. Generation of multi-photon correlated states using combination of second harmonic generation nonlinear process together with parametric down-conversion and eventually using an attenuated coherent beams has several significant advantages against other methods, particularly no need for cryogenic experimental technique, high collection efficiency, and well defined wavelength of generated photons.

The applicability of the multi-photon source for any information protocol requires precise definition of generated photons in all their degrees of freedom. Since almost all protocols exploit the interference the mutual indistinguishability is extremely important.

Chapter 2

Generation of multi-photon correlated states

2.1 Spontaneous parametric down conversion

Parametric fluorescence or spontaneous parametric down conversion (SPDC) is the nonlinear optical process whereby two photons are created from a single pump photon. A nonlinear medium splits incoming photons into pairs of photons of lower frequency called signal and idler. "Parametric" refers to the fact that the state of the nonlinear medium is left unchanged and thus energy and momentum of interacting photons must be conserved. "Spontaneous" refers to the fact that the process is stimulated by random vacuum fluctuations. At present, SPDC is the most accessible and controllable source of entanglement. This source has been essential tool in variety of quantum-mechanical and information experiments, such as in testing Bell-inequalities, teleportation, entanglement swapping, and dense coding, as well as in quantum cryptography and quantum computation.

SPDC can be treated as three photon process where the crystal with nonlinearity of second order is illuminated by a pump beam. The pump beam should be intense enough to drive the oscillations of the electrons in the medium in nonlinear regime. For strong beams the nonlinear phenomenon of parametric down-conversion can be understood by the semiclassical theory of electro-magnetic field. At low light intensities a quantum mechanical description of the interaction should be utilized because it leads to nonclassical effects such as squeezing of phase quadratures of light or spontaneous production of correlated photon pairs.

2.1.1 Multimode perturbative treatment

Following the [9] the effective Hamiltonian for the parametric down conversion process in the interaction picture can be written as

$$H_{\mathrm{I}}(t) = \frac{1}{L^3} \sum_{\mathbf{k}',s'} \sum_{\mathbf{k}'',s''} V_l \chi^{(2)}_{lij}(\omega_{\mathrm{p}}, \omega', \omega'')(\epsilon^*_{\mathbf{k}'s'})_i (\epsilon^*_{\mathbf{k}''s''})_j$$
$$\times \int_{\mathcal{V}} e^{i(\mathbf{k}_{\mathrm{p}} - \mathbf{k}' - \mathbf{k}'')} e^{i(\omega' + \omega'' - \omega_p)t} \hat{a}^+_{\mathbf{k}'s'} \hat{a}^+_{\mathbf{k}''s''} \mathrm{d}^3 r + \mathrm{H.c.}, \tag{2.1}$$

where $\chi^{(2)}_{lij}$ is the nonlinear electric susceptibility tensor and indices l, i, j denote vector components. Integration is performed over the volume of the crystal $\mathcal{V}$. The generated fields are quantized while the pump beam is treated classically. Pump beam is taken to be monochromatic wave of vector amplitude $\mathbf{V}$, wave vector $\mathbf{k_p}$ and frequency ω_p. Length of the quantization box is L and vectors ϵ describe the polarization of individual modes. Operator $\hat{a}_{\mathbf{k}'s'}$ annihilates particle in mode with wave vector $\mathbf{k}$ and index s' and satisfy a common commutation relation $[\hat{a}_{\mathbf{k}'s'}, \hat{a}_{\mathbf{k}''s''}] = \delta_{\mathbf{k}'\mathbf{k}''}\delta_{s's''}$. If the initial state of the field in interaction picture is the vacuum state $|\Psi(0)\rangle = |0\rangle_s |0\rangle_i$, the two-photon quantum state $|\Psi(t)\rangle$ at the output of the nonlinear medium at later time t is given by

$$|\Psi(t)\rangle = \exp\left[-\frac{i}{\hbar}\int_0^t H_I(t')\right]|\Psi(0)\rangle \mathrm{d}t'. \tag{2.2}$$

The state at the output of the crystal after performing the integration over spatial and time variables within the first-order perturbation theory with the restriction to the first two terms can be written as

$$|\Psi(t)\rangle = M|0\rangle_s|0\rangle_i + \frac{\eta\delta\omega}{2\pi}\sum_{\omega'}\sum_{\omega''}\phi(\omega',\omega'')\frac{\sin[\frac{1}{2}(\omega' + \omega'' - \omega_{\mathrm{p}})t]}{\frac{1}{2}(\omega' + \omega'' - \omega_{\mathrm{p}})}$$
$$\times e^{\frac{i}{2}(\omega' + \omega'' - \omega_{\mathrm{p}})t/2} \hat{a}^+_s(\omega')\hat{a}^+_i(\omega'')|0\rangle_s|0\rangle_i, \tag{2.3}$$

where M and η are normalization constants which can be evaluated easily after assuming that $|\phi(\omega', \omega'')|^2$ is a constant, that is fulfilled in most practical cases because it is slowly varying with respect to the sinc function. In the derivation of Eq. (2.3) the similar polarizations of signal and idler photons are assumed. Directions of signal and idler modes are in practice well defined by apertures, that is, the directions of $\mathbf{k}'$ and $\mathbf{k}''$ are fixed and only sum over frequencies of signal and idler modes remains. The coefficient $\phi(\omega', \omega'')$ is often called two-photon spectral function because it express the frequency dependence of factors under the sum. Two-photon spectral function is taken to be symmetric with respect to frequencies ω' and ω'' and reach its maximal value at $\omega' = \omega'' = \omega_{\mathrm{p}}/2$. The mode spacing $\delta\omega$ arise from finite modes in quantization volume L^3 and in the limit of infinity large quantization box goes to zero and sums over frequencies can be replaced by integrals.

As can be seen in Eq. (2.3), the state $|1,1\rangle$ is generated in the modes s and i with wave vectors k_{i} and k_{s} at the output of the crystal surface, respectively. The important feature of

such state is simultaneous generation of the photons, i.e. photons are generated in pairs. If photon in one of involved separated modes is detected, for example in signal mode, then the corresponding photon from the pair is present with high probability in the complementary idler mode. The heralding probability is proportional to two-photon coupling efficiency η defined as [10]

$$\eta = \frac{N_{\text{coinc}}}{\sqrt{N_{\text{s}} N_{\text{i}}}}, \tag{2.4}$$

where N_s and N_i are the numbers of detection events in the signal and idler arms, respectively, and N_c corresponds to simultaneous detection at both detectors, i.e. number of coincidences.

2.1.2 Phase matching

The down-converted photons are produced almost simultaneously. Momentum and energy conservation requires that the wave vector $\mathbf{k}_{\text{p}}$ and frequency ω_{p} of pump photon equal to sum of wave vectors $\mathbf{k}_{\text{s}}, \mathbf{k}_{\text{i}}$ and frequencies $\omega_{\text{s}}, \omega_{\text{i}}$ of generated photons,

$$\mathbf{k}_{\text{p}} = \mathbf{k}_{\text{s}} + \mathbf{k}_{\text{i}} \qquad \text{and} \qquad \omega_{\text{p}} = \omega_{\text{s}} + \omega_{\text{i}}, \tag{2.5}$$

respectively. This equations are called the phase-matching conditions. SPDC phase-matching can be divided to two types with respect to polarization of generated photons. In type-I phase-matching the generated signal and idler photons are in the same polarization state while in type-II their polarization states are orthogonal.

For type-I degenerate non-collinear phase matching equations (2.5) reduce to

$$n(\lambda_{\text{p}}, \theta) = n(2\lambda_{\text{p}}) \cos \alpha, \tag{2.6}$$

where θ is the angle between crystal optical axis and direction of pumping beam and α is angle determining the propagation direction of generated photons with respect to pump wave, see Fig. 2.1. Phase matching can be satisfied for example in birefringent materials, i.e. materials where $n_{\text{o}}(\lambda) \neq n_{\text{e}}(\lambda)$. Here o and e denote ordinary and extraordinary polarized waves, respectively. In our experiment the negative uniaxial crystal with $n_{\text{o}}(\lambda) > n_{\text{e}}(\lambda)$ is employed to achieve the interaction e $\rightarrow$ oo between a three interacting waves. For fixed frequency ω_{p} of the pump wave and desired output angle $\beta = \arcsin[n_{\text{o},\omega_{\text{p}}/2} \sin(\alpha(\theta))]$ of generated photons the proper cut and tilt of the crystal can be computed using elliptical parametrization of $n_{\text{e},\omega_{\text{p}}}$

$$\frac{1}{n_{\text{e},\omega_{\text{p}}}^2(\theta)} = \frac{\cos^2 \theta}{n_{\text{o},\omega_{\text{p}}}^2} + \frac{\sin^2 \theta}{n_{\text{e},\omega_{\text{p}}}^2}. \tag{2.7}$$

Principal indices of refraction $n_{\text{o},\omega_{\text{p}}}$ and $n_{\text{e},\omega_{\text{p}}}$ can be computed using Sellmeier equations for given material.
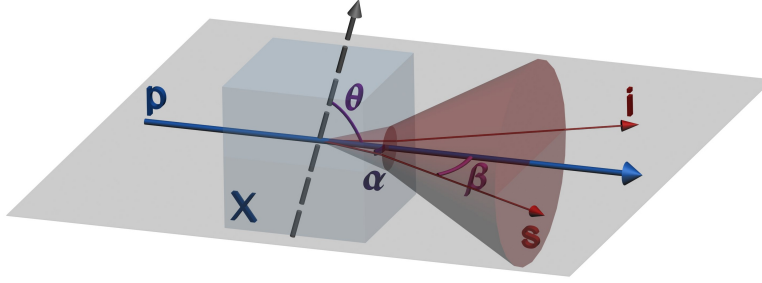
Figure 2.1: The SPDC type-I scheme. Crystal with second order nonlinearity is illuminated by pump beam p. Generated degenerate pairs of photons are distributed in the cone. The half-angles of the cone are denoted as α and β inside and outside of the crystal, respectively.

2.1.3 Pulsed pumping

In contrast to continuous wave (CW) pumping, where the wavelength spectrum of the pumping photon is extremely narrow and can be well approximated by Dirac δ-function, several important effects arise in the SPDC pumped by pulses with finite spectral and temporal width. The convenient fundamental laser source for applications of multi-photon generation is femtosecond laser. The spectrum of the frequency doubled pumping photons has for femtosecond pulses bandwidth typically several nanometers.

The spectrum width of pulsed pumped SPDC photons emitted in the angle spread $\Delta\beta$ is several times wider than in the CW pumping case due to the widening of the longitudinal spectrum. This effect can be well illustrated by so-called tuning curves. Tuning curves are graphical representations of the angle β of generated photons as a function of their wavelength, see Fig. 2.2. They can be computed directly by evaluating the phase matching conditions (2.5) for given crystal tilt θ and pump wavelength λ_p. Tuning curves represent very useful relations because one can easily deduce the bandwidth of collected pairs. While the spectrum coupled into angle spread $\Delta\beta$ for CW pumping is tens of nanometers it is roughly ten times wider for pulsed pumping with pump bandwidth of 2 nanometers. The impact of the finite bandwidth of pumping pulse on the heralding efficiency illustrated using tuning curves is discussed in [11].

In the case of pulsed pumping the non-normalized two photon state of SPDC photon pair can be with the help of (2.3) defined as

$$|\Psi_{\text{SPDC}}\rangle = \int d\omega_p g(\omega_p) e^{i\omega_p \tau_p} \int d\omega' \int d\omega'' \delta(\omega' + \omega'' - \omega_p) \hat{a}_s^+(\omega') \hat{a}_i^+(\omega'') |0\rangle_s |0\rangle_i, \qquad (2.8)$$

where the first integral is taken over the pump beam frequency distribution $g(\omega_p)$ and τ_p is the arrival time of the pump pulse into the nonlinear medium. The sums in the (2.3) have been replaced by integrals thus the mode spacing $\delta\omega$ vanished. The sinc function was replaced by Dirac δ-function because in most practical realizations as well as in our experiment, the length of nonlinear medium is sufficiently short to make this assumption. The vacuum contributions
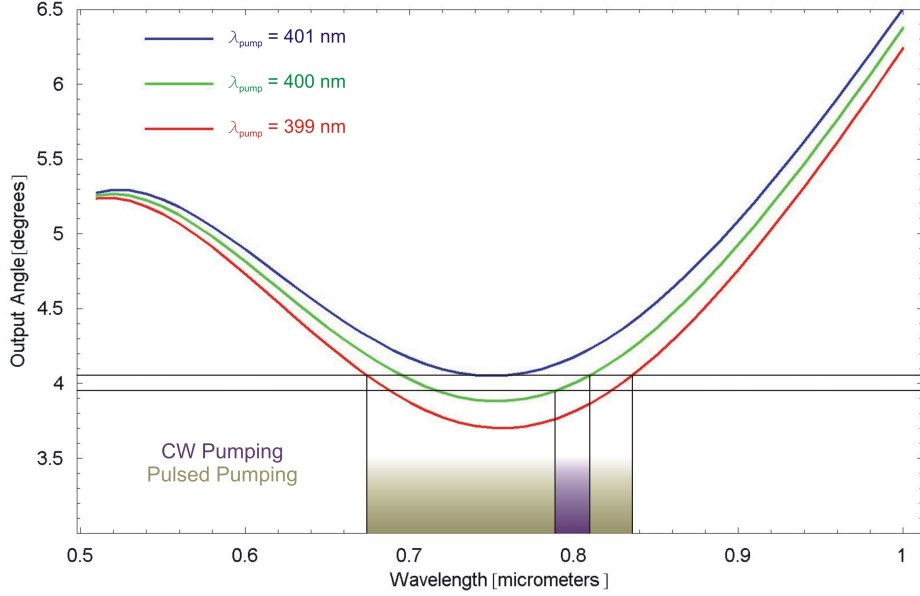
10

Figure 2.2: Example of SPDC tuning curves evaluated for $\lambda_p = 400\,\text{nm}$, $\theta = 29.8\,\text{degrees}$ and signal photons. The angle spread $\Delta\beta$ is centered at $4\,\text{degrees}$ that is the output angle of photons with wavelength of $800\,\text{nm}$. The curves are identical for idler photons.

have been omitted because they do not contribute to photon detections. The detailed computation of two-photon spectral function $\phi(\omega', \omega'')$ in pulsed pumping case for both type I and II SPDC including higher terms of the wave-number expansion can be found in [12, 13, 14]. However, presented description gives very accurate results particularly for the SPDC type I and narrow bandwidth filters before the detectors.

2.2   Attenuated coherent beam

Another approach of generating single photon states is based on attenuating coherent beam to the single-photon level. The big advantage of this approach is relatively simple preparation of the state, because the coherent state can be obtained directly from the laser. The coherent state $|\alpha\rangle$ is an eigenstate of the annihilation operator $\hat{a}$, $\hat{a}|\alpha\rangle = \alpha|\alpha\rangle$ and can be expressed in the Fock-state basis as

$$|\alpha\rangle = \exp\left(-\frac{1}{2}|\alpha|^2\right) \sum_{n=0}^{\infty} \frac{\alpha^n}{\sqrt{n!}}|n\rangle. \tag{2.9}$$

Thus, its overlap with the state $|n\rangle$ containing exactly n photons is

$$P(n, \alpha) = |\langle n|\alpha\rangle|^2 = \frac{|\alpha|^{2n}}{n!}\exp\left(-|\alpha|^2\right). \tag{2.10}$$

Equation (2.10) represents Poisson distribution with the mean number of photons $\langle n \rangle = |\alpha|^2$ describing the probability $P(n, \alpha)$ of finding n photons in the coherent state. For $n = 1$,

i.e. the probability of finding exactly one photon in the coherent state, the equation (2.10) reduces to $P(1, \alpha) = |\alpha|^2 \exp\left(|\alpha|^2\right)$. As one would expect, the probability $P(1, \alpha)$ is peaked for $|\alpha|^2 = 1$, where its maximal value reaches P(1)=36.8 %, see Fig. 2.3 (a). That is not very satisfactory result, however, in most practical realizations photons are manipulated and detected and only events where one or more photons are detected are taking into the account. Thanks to such postselection the vacuum state in Eq. (2.9) can be neglected because it does not contribute to successful detections by common photon counters described by normally ordered detection operators. After normalization the overlap of such state $|\alpha - 0\rangle$ with n-photon state $|n\rangle$ is given by

$$P_0(n, \alpha) = |\langle n|\alpha - 0\rangle|^2 = \frac{|\alpha|^{2n}}{(e^{|\alpha|^2} - 1)n!}. \tag{2.11}$$

For low coherent beam intensity $|\alpha|^2$ the probability $P_0(1, \alpha) \to 1$, as can be seen in Fig. 2.3 (b).
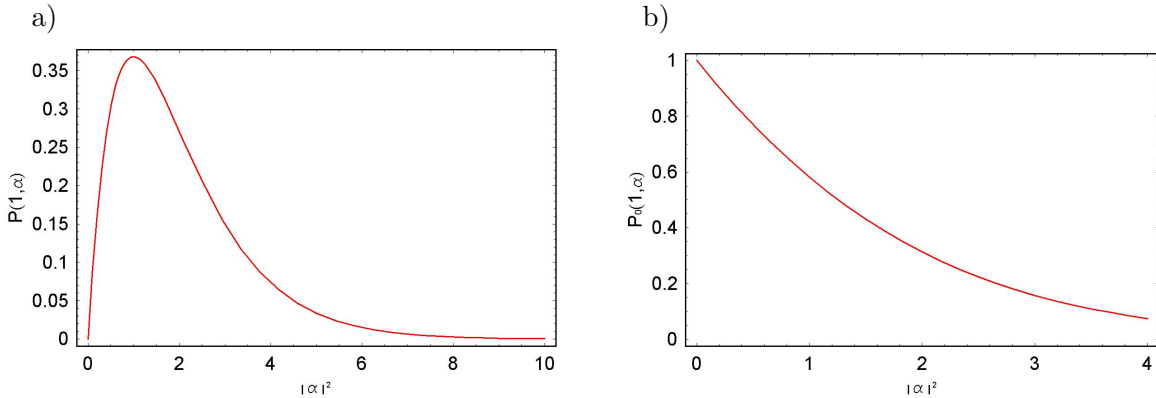
a)
b)

Figure 2.3: The overlap of single photon state $|1\rangle$ with coherent state $|\alpha\rangle$ and with state $|\alpha - 0\rangle$ as a function of coherent beam intensity $|\alpha|^2$.

2.3 Multi-photon interference

2.3.1 Two-photon interference

Hong-Ou-Mandel (HOM) effect is the most famous two-photon interference effect. It is widely exploited in the field of quantum information processing. HOM interference serves as the essential process in the linear optics quantum computing schemes [15]. HOM interference is fourth order interference effect named after authors of its first experimental realization [16]. In HOM interference two photons are mixed on the beam splitter. If there is no possibility to distinguish incoming photons in any of their degrees of freedom, they experience destructive interference and leave the beam splitter together in the same output mode.

Consider a beam splitter with input modes a_{in}, b_{in} and output modes a_{out}, b_{in} depicted at Fig. 2.6. Suppose that in each input mode is one photon so the initial state can be written as
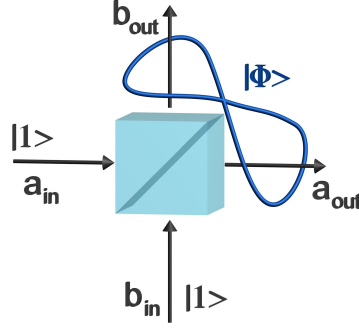
Figure 2.4: The basic scheme of the beam splitter, which provides the unitary mixing operation on the input modes.

$$|\Phi\rangle_{\text{in}} = \hat{a}_{\text{in}}^{+}\hat{b}_{\text{in}}^{+}|0\rangle_{a}|0\rangle_{b}. \tag{2.12}$$

The action of the lossless beam splitter is described in the Heisenberg picture by unitary transformation of creation operators of input modes [17],

$$\begin{pmatrix} \hat{a}_{\text{out}}^{+} \\ \hat{b}_{\text{out}}^{+} \end{pmatrix} = U_{\text{BS}} \begin{pmatrix} \hat{a}_{\text{in}}^{+} \\ \hat{b}_{\text{in}}^{+} \end{pmatrix} = \begin{pmatrix} \tau & \rho \\ -\rho & \tau \end{pmatrix} \begin{pmatrix} \hat{a}_{\text{in}}^{+} \\ \hat{b}_{\text{in}}^{+} \end{pmatrix}, \tag{2.13}$$

where ρ and τ are amplitude reflectivity and transmissivity, respectively. By taking the inverse of the beam splitter matrix U_{BS} we have

$$\hat{a}_{\text{in}}^{+} \rightarrow \tau\hat{a}_{\text{out}}^{+} - \rho\hat{b}_{\text{out}}^{+} \qquad \text{and} \qquad \hat{b}_{\text{in}}^{+} \rightarrow \rho\hat{a}_{\text{out}}^{+} + \tau\hat{b}_{\text{out}}^{+}. \tag{2.14}$$

Therefore the input state (2.12) transforms as follows,

$$|\Phi\rangle_{\text{in}} \rightarrow |\Phi\rangle_{\text{out}} = (\tau\hat{a}_{\text{out}}^{+} - \rho\hat{b}_{\text{out}}^{+})(\rho\hat{a}_{\text{out}}^{+} + \tau\hat{b}_{\text{out}}^{+})|0,0\rangle =$$
$$= \tau\rho\sqrt{2}|2,0\rangle - \tau\rho\sqrt{2}|0,2\rangle + \tau^{2}|1,1\rangle - \rho^{2}|1,1\rangle. \tag{2.15}$$

For the balanced beam splitter $\rho = \tau = \frac{1}{\sqrt{2}}$ amplitudes of states $|1,1\rangle$ interferes destructively, that is, the probability of simultaneous detection of photon in both beam splitter output ports goes to zero. The coincidence rate is zero for two identical, indistinguishable, and simultaneously incident photons. Therefore, the superposition $|\Phi\rangle$ of states $|2,0\rangle$ and $|0,2\rangle$ with equal amplitudes is generated at the output of the beam splitter. This superposition represents the particular case of highly nonclassical NOON state which can be written as the superposition $|N,0\rangle + e^{i\phi}|0,N\rangle$ [18]. Beam splitter can be used also for generation of entanglement in other degrees of freedom, for example polarization entanglement.

Let us consider scheme depicted at Fig. 2.5. Assume that mutually perfectly indistinguishable photons are again at the both input ports. Precise variable time delay $\Delta\tau$ is placed in one input mode. The photo-detectors are placed in the both output ports of beamsplitter after the bandwidth filters with frequency response functions $f_i(\omega)$ and their output pulses are

processed by coincidence logics (CC) with time window of several nanoseconds. In practice the frequency response of the photo-detectors is much broader than the transmission curve of the bandwidth filters, thus their efficiency can be treated as frequency independent. For simplicity the quantum efficiencies of detectors are taken to be unity in this calculation. The
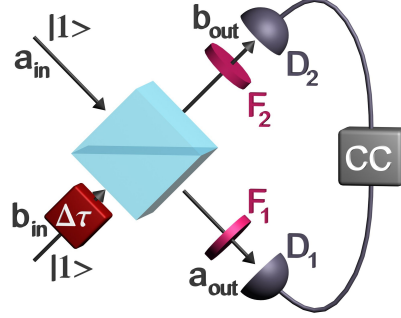

Figure 2.5: The scheme of measuring the two-photon coincidences in dependence of time delay $\Delta\tau$ between the incoming photons.

amplitude for the detector D_i ($i = 1, 2$) to detect a photon at time t is given by the transition amplitude [19]

$$A^{(i)}(t) = \langle 0|E_i^{(+)}(t)|\Psi\rangle, \tag{2.16}$$

where $|\Psi\rangle$ is the state of the field incident on the detector. Similarly the probability amplitude for a coincidence event, i.e. detection of one photon by detector D_1 at time t_1 and one by detector D_2 at t_2 can be written as

$$A_2^{(1,2)}(t_1, t_2) = \langle 0|E_1^{(+)}(t_1)E_2^{(+)}(t_2)|\Psi\rangle. \tag{2.17}$$

The $E_i^{(+)}(t)$ is the positive frequency part of the electromagnetic field operator weighted by the frequency-response function of the bandwidth filter $f_i(\omega)$ at the detector D_i,

$$E_i^{(+)}(t_i) = \int d\omega\, f_i(\omega)e^{-i\omega t_i}\hat{a}_i(\omega). \tag{2.18}$$

By combining the equations describing the beam splitter operation on creation operators (2.14) with the state of down-converted pair (2.8) the output SPDC state is,

$$|\Psi_{\mathrm{SPDC}}\rangle = \frac{1}{2}\int d\omega_s \int d\omega_i g(\omega_s + \omega_i)e^{i\omega_s\tau_P}e^{i\omega_i(\tau_P+\Delta\tau)}(\hat{a}_1^+(\omega_s)\hat{a}_1^+(\omega_i)+$$
$$+\hat{a}_1^+(\omega_s)\hat{a}_2^+(\omega_i) - \hat{a}_2^+(\omega_s)\hat{a}_1^+(\omega_i) - \hat{a}_2^+(\omega_s)\hat{a}_2^+(\omega_i))|0,0\rangle, \tag{2.19}$$

where the $\Delta\tau$ is the time delay between the signal and idler photons at the beam splitter. The assumption of Gaussian shapes of the spectral filters responses and pump-pulse spectrum is well fulfilled in most of practical realizations,

$$g(\omega_p) = \frac{1}{\sqrt{2\pi}\sigma_p}e^{-\frac{(\omega_p - \omega_{p0})}{2\sigma_p^2}} \qquad \text{and} \qquad f_i(\omega) = f_{i0}e^{-\frac{(\omega - \omega_{fi0})^2}{2\sigma_{fi}^2}}. \tag{2.20}$$

Here σ_p and σ_fi are the RMS bandwidths of pump pulse and filter in arm i, respectively, while the ω_p0 and ω_fi0 denote their center frequencies and f_i0^2 is the peak transmissivity of employed filters. After combining the equations form (2.17) to (2.20), applying the standard commutation relations for creation operators and performing the integration with respect to the frequencies in both modes, the twofold coincidence event probability amplitude as the function of detection times t_1, t_2 and time delay $\Delta\tau$ is obtained. Let's assume for simplicity that the $\omega_0 = \omega_\mathrm{fi0} = \frac{\omega_\mathrm{p0}}{2}$, $f_0 = f_{10} = f_{20}$ and $\sigma_\mathrm{f} = \sigma_\mathrm{f1} = \sigma_\mathrm{f2}$. The coincidence probability is obtained by taking the square modulus of the twofold coincidence amplitude, integrating over the detection times t_1 and t_2 and normalization of resulting term,

$$P_{1,2}(\Delta\tau) = 1 - e^{-\frac{1}{2}\sigma_\mathrm{f}^2 \Delta\tau^2}. \tag{2.21}$$

Therefore, the probability of coincidence detection $P_{1,2}(\Delta\tau)$ in computed simplified case is the Gaussian function and vanishes for $\Delta\tau \to 0$.

The HOM interference quality can be well described by the visibility V defined as

$$V = \frac{N_\mathrm{max} - N_\mathrm{min}}{N_\mathrm{max} + N_\mathrm{min}}, \tag{2.22}$$

where N_max and N_min are the minimum and maximum number of coincidences, respectively. Visibility $V \in \langle 0, 1 \rangle$ and is the crucial parameter through the rest of thesis, because describes through the quality of the interference also the quality of the photon sources.

2.3.2 Three-photon interference

The interference of the weak coherent beam with single photons at the beam splitter has been demonstrated by Rarity and Tapster in 1997 [20]. This source type has been extensively employed in several quantum optics experiments by Franson and Pittman group during last three years, for example [21, 22, 23, 24].

The coherent beam attenuated to a single photon level interacts with single photon prepared by triggering on the second photon from SPDC pair. Similarly to two-photon interference if there is no possibility to distinguish the interfering photons they leave the beam splitter by the same output port. Using the beam splitter transformation (2.14) and the coherent state decomposition into the Fock states basis (2.9) the computed coincidence probability P_c can be written as a function of the coherent beam intensity $|\alpha|^2$,

$$P_\mathrm{c} = 1 - e^{-\frac{|\alpha|^2}{2}} - \frac{1}{2}|\alpha|^2 e^{-\frac{|\alpha|^2}{2}} \mathcal{O}, \tag{2.23}$$

where $\mathcal{O}$ is the overlap of interacting photons. Then the visibility V expressed as a function of $|\alpha|^2$ has the form

$$V = \frac{|\alpha|^2}{4(e^{\frac{|\alpha|^2}{2}} - 1) - |\alpha|^2}. \tag{2.24}$$

15

The equation (2.24) suggests that for weak coherent beam where the probability of the photon in particular pulse is low the visibility $V \to 1$ while for high intensities the interference vanishes and $V \to 0$. Therefore, in practice one should always search for some optimal value of $|\alpha|^2$ to
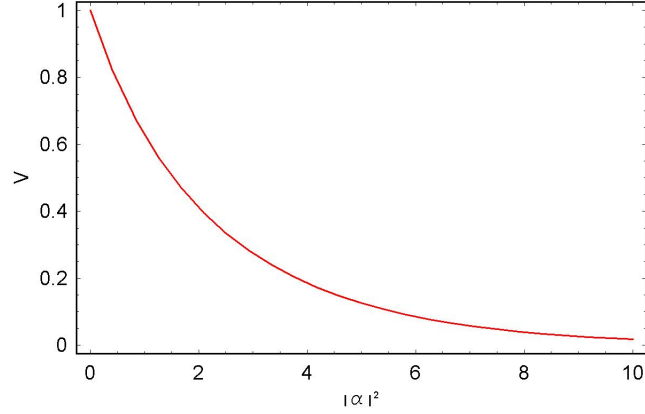

Figure 2.6: The interference visibility as a function of the coherent state intensity $|\alpha|^2$.

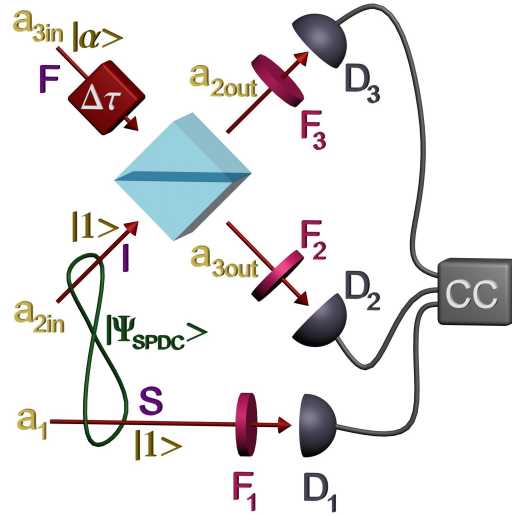reach both acceptable rate and sufficient visibility.

Figure 2.7: Scheme of the three-photon interference.

Suppose that the SPDC spatially separated photons S and I are in modes a_1 and $a_{2\mathrm{in}}$, respectively, while the photon F from attenuated coherent laser beam is in mode $a_{3\mathrm{in}}$, see Fig. 2.7. The modes $a_{2\mathrm{in}}$ and $a_{3\mathrm{in}}$ are mixed on the balanced beamsplitter after precise setting of their mutual time delay $\Delta\tau$. The output beam splitter modes $a_{2\mathrm{out}}$ and $a_{3\mathrm{out}}$ as well as mode a_1 are spectrally filtered by bandwidth filters and detected by photo-detectors. Photo-detectors outputs are processed by coincidence logic and counter (CC). For the sake of simplicity the coherent state $|\alpha\rangle$ can be replaced by the single photon state $|1\rangle$. This assumption is equivalent to the the very low coherent beam intensity that is fulfilled in the

experiment. The input three-photon state can be with the help of (2.8) written as,

$$|\zeta\rangle_{\text{in}} = |\Psi_{\text{SPDC}}\rangle|1_{\text{F}}\rangle = \int d\omega_{\text{F}} \int d\omega_{\text{s}} \int d\omega_{\text{i}} g(\omega_{\text{s}} + \omega_{\text{i}}) e^{i(\omega_{\text{s}} + \omega_{\text{i}})\tau_{\text{P}}} h(\omega_{\text{F}}) e^{i\omega_{\text{F}}(\tau_{\text{F}} + \Delta\tau)}$$
$$\times \hat{a}_1^+(\omega_s) \hat{a}_{2\text{in}}^+(\omega_i) \hat{a}_{3\text{in}}^+(\omega_F) |\text{vac}\rangle, \tag{2.25}$$

where the additional integral is taken over the coherent beam frequency distribution $h(\omega_F)$ and τ_F is the time corresponding to the coherent photon generation. All three photons pass the bandwidth filters and are detected by photo-detectors. The probability amplitude for a threefold coincidence event can be by analogy to (2.17) expressed as,

$$A_3^{(1,2,3)}(t_1, t_2, t_3) = \langle 0|E_1^{(+)}(t_1) E_2^{(+)}(t_2) E_3^{(+)}(t_3)|\zeta\rangle_{\text{out}}, \tag{2.26}$$

where $|\zeta\rangle_{\text{out}}$ is the three-photon state after the beam splitter obtained by transforming the $\hat{a}_{2\text{in}}^+(\omega_i)\hat{a}_{3\text{in}}^+(\omega_F)$ in (2.25) according to (2.14). Let us assume the Gaussian shapes of the bandwidth filters functions and pump-pulse spectrum defined in (2.20) and similarly defined Gaussian shape of the coherent beam spectrum with RMS bandwidth σ_F and center frequency $\omega_{\text{F}0}$. Following the procedure from previous section the three-photon probability amplitude can be computed. After assuming the same simplifications, i.e. $\omega_0 = \omega_{\text{fi}0} = \frac{\omega_{\text{p}0}}{2} = \omega_{\text{F}0}$, $f_0 = f_{10} = f_{20} = f_{30}$ and $\sigma_{\text{f}} = \sigma_{\text{f}1} = \sigma_{\text{f}2} = \sigma_{\text{f}3}$, the coincidence probability can be computed by taking the square modulus of the threefold coincidence amplitude and integrating over the detection times t_1 and t_2 and t_3. The resulting normalized threefold coincidence probability in the dependence of $\Delta\tau$ has again the Gaussian form,

$$P_{1,2,3}(\Delta\tau) = 1 - N(\sigma_{\text{f}}, \sigma_{\text{p}}, \sigma_{\text{F}}) e^{-\frac{\Delta\tau^2}{2\sigma(\sigma_{\text{f}}, \sigma_{\text{p}}, \sigma_{\text{F}})^2}}. \tag{2.27}$$

In contrast to the two-photon case (2.21), the three-photon interference visibility depends on the bandwidths of the filters, pump pulse, and coherent beam. The constant $N(\sigma_{\text{f}}, \sigma_{\text{p}}, \sigma_{\text{F}})$ is given by

$$N(\sigma_{\text{f}}, \sigma_{\text{p}}, \sigma_{\text{F}}) = \frac{2\sigma_{\text{F}}\sigma_{\text{p}}\sqrt{(\sigma_{\text{f}}^2 + \sigma_{\text{F}}^2)(2\sigma_{\text{f}}^2 + \sigma_{\text{p}}^2)}}{\sqrt{(2\sigma_{\text{F}}^2\sigma_{\text{p}}^2 + \sigma_{\text{f}}^2(\sigma_{\text{F}}^2 + \sigma_{\text{p}}^2))(\sigma_{\text{f}}^4 + 2\sigma_{\text{F}}^2\sigma_{\text{p}}^2 + \sigma_{\text{f}}^2(3\sigma_{\text{F}}^2 + \sigma_{\text{p}}^2))}}. \tag{2.28}$$

The width of the three-photon dip depends also on all three mentioned bandwidths, not only on the bandwith of the interference filters,

$$\sigma(\sigma_{\text{f}}, \sigma_{\text{p}}, \sigma_{\text{F}}) = \sqrt{\frac{2\sigma_{\text{F}}^2\sigma_{\text{p}}^2 + \sigma_{\text{f}}^2(\sigma_{\text{F}}^2 + \sigma_{\text{p}}^2)}{2\sigma_{\text{f}}^2\sigma_{\text{F}}^2\sigma_{\text{p}}^2}}. \tag{2.29}$$

2.4 Indistinguishability of interacting photons

Complementary principle of quantum mechanics states that distinguishability degrades the quality of interference that manifests itself by the reduction of the visibility. Satisfying the

indistinguishability of interfering particles in all their degrees of freedom is challenging task especially for the multi-photon interference of photons coming from independent sources. In general four main parameters of interacting photons have to be matched, namely the spatial modes, temporal and spectral parameters, and polarization modes.

2.4.1 Spatial mode definition

The precise definition and matching of interacting beams are the necessary conditions for high visibility of non-classical interference [25, 26, 27]. Due to difference in spatial modes structure of interfering beams the photons can be in principle distinguished by measurement of their spatial properties. Further, the precise definition of spatial pump mode enables the alignment of SPDC setup and determines the correlation area of generated photons. Due to the nonlinearity of the SHG process, strong focusing, and abberations of optical elements the output beam suffers from very irregular spatial structure far away from purity of the fundamental beam. Fortunately, the spatial properties can be improved by transmitting only selected parts of the beam—the spatial filtering. In the presented multi-photon source based on the SPDC and attenuated coherent beams the frequency doubled beam and SPDC generated photons need undergo spatial filtering.

Optical beam, particularly the one generated by a nonlinear process, consists in general of many coaxial spatial modes with different propagation and mutual-coherence properties. The structure of the beam can be described by superposition of orthogonal modes in which the lowest one represents the fundamental mode, usually with Gaussian intensity profile. For purpose of this work the spatial filter is defined as a device transmitting, in the ideal case, only the fundamental mode. Optical power P_{out} of the output beam compared to the total input power P_{in} determines the *filtering efficiency*, $\eta = P_{\text{out}}/P_{\text{in}}$, that depends on the spatial filter as well as on the structure of the input beam. The *quality* of the output beam U_{out} is given by its overlap η_{ovrl} with the desired output mode U_{design} that will be the Gaussian one in the rest of this work,

$$\eta_{\text{ovrl}} = \left| \int \mathrm{d}x\, U_{\text{design}}^*(x)\, U_{\text{out}}(x) \right|^2 . \tag{2.30}$$

For generic multimode beam described by second order correlation function $\rho_{\text{out}}(x, x') = \sum_n \lambda_n U(x) U^*(x')$ the overlap with the mode U_{design} reads

$$\eta_{\text{ovrl}} = \int \int \mathrm{d}x\, \mathrm{d}x'\, U_{\text{design}}^*(x)\, U_{\text{design}}(x')\, \rho_{\text{out}}(x, x'). \tag{2.31}$$

The quality of spatial filtering depends on the employed filter scheme. Coupling the input beam into a single-mode (SM) optical fiber represents conceptually simple method for spatial filtering based on rapid attenuation of higher modes during the propagation through the SM fiber [28]. The fundamental LP_{01} mode guided and transmitted practically without losses matches the Gaussian mode with the overlap $\eta_{\text{ovrl}} = 99.63$ % yielding almost perfect quality

of the output beam. The filtering efficiency is given basically by overlap of the input beam and the guided mode. Obviously, the filtering efficiency could be as high as 99.63 % for single-mode Gaussian beam at the input. However, the maximum filtering efficiency $\eta_{\max} \approx 85$ % can be reached due to power losses of optical components used for coupling into the fiber and Fresnel reflection at fiber end faces [29]. After correcting on these imperfections, the measured filtering efficiency for generic input beam yields its overlap with the Gaussian mode. In this way, the quality of spatial filtering for any spatial filter can be experimentally measured by coupling the output filtered beam into the SM fiber.

Another feasible method of spatial filtering consist in low-pass filtering of spatial Fourier spectrum by a circular pinhole by means of well known 4-f system. For input beam width (at the pinhole entrance) smaller than pinhole diameter the beam passes through the system almost unfiltered. Conversely, for approximately flat intensity profile of the input beam at the pinhole entrance, the output beam intensity resembles the common "besinc" diffraction pattern, $[J_1(x)/x]^2$, yielding the output mode quality of 81.5 %. However, after selecting only central part of the diffracted beam up to the first intensity minimum, the overlap of the output filtered beam and Gaussian mode reaches $\eta_{\mathrm{ovrl}} = 98.8$ %. Thus, removing the side intensity maxima increases the quality of spatial filtering by 17 % at the expense of additional 16 % of power losses.

The filtering efficiency of the 4-f system is again given basically by overlap of the input beam and the transmitted mode described in this case by the central part of besinc function. Unfortunately, this output mode slightly depends on the mode structure of the input beam, even for wide beam impinging the smaller pinhole, which yields the nonlinear relation. Together with non-perfectly circular shape of the pinhole and abberations of used lenses the total filtering efficiency cannot be predicted exactly. However, it can be set by proper design of 4-f spatial filter to be approximately equal to filtering efficiency obtained for the same input beam filtered by SM fiber. This assures high quality filtering without excessive losses especially in the real case where the input beam structure is not known in detail.

2.4.2 Temporal and spectral mode matching

The distinguishability of interfering photons highly depends on their temporal and spectral overlap [30]. Temporal distinguishability diminish the interference if their arrival times at the beam splitter are different. That is obvious from the calculations in Section 2.3.1 where the HOM interference visibility rapidly decreases for the time difference of the incoming photons at the scales of their pulse lengths. Therefore for the high visibility one has to set the paths lengths of interfering photons equal each to other with the precision higher than their pulse widths. In practice it often means to match the several meters long paths in various materials with the precision tens of micrometers. Temporal overlap can decrease the visibility also if the arm lengths are perfectly identical due to the different time shapes and lengths of the

overlapped photons. That is not the case of the HOM interference between photons from SPDC which pass the similar optical components, however in the case of the photons coming from the partly independent sources with different temporal modes which pass different dispersive elements it is practically often considerable contribution to distinguishability.

In the case of Fourier transform-limited pulses, i.e. the pulses which are as short as their spectral bandwidth allows, the pulse lengths are precisely defined by the bandwidth of used interference filters. Therefore, for the similar spectral filtering of all employed modes the overlaps of both the temporal and the spectral mode functions are perfect. However, the propagation in the dispersive optical components or even components with optical nonlinearities causes the spectral chirp and thus leads to Fourier non-transform-limited pulses. The pulse lengths then vary in dependence of the path that yields different pulse lengths and frequency chirps. For the two photon interference the chirp of the pumping pulse in most of the experimental setups does not decrease interference visibility, because photons coming from the same SPDC pair experience the same pumping pulse length, shape, and spectral distribution.

In the interference of photons coming from the independent sources, particularly in the case of the Rarity-Tapster type interference, the one of interfering photons undergoes the SHG and SPDC processes while the other does not experience none of them. Interacting photons also experience different dispersion due to the various path lengths in the various optical components. Differences in dispersion mediums and their lengths change the temporal profile and eventually also spectral distribution within the pulses differently, that clearly lower the time and spectral overlap in the interference. Moreover, due to the depletion of fundamental pulse in the SHG process, temporal mode of fundamental pulse changes its shape. The group velocity mismatch (GVM) in both SHG and SPDC crystals give rise to the timing jitter of the generated pulses. The GVM is effect caused by different group velocities of the pumping and generated photons. The pumping photons can be converted at each point of the crystal. Due to the different propagation velocities of pumping and generated photons they acquire a mutual time delay. The generated SHG and SPDC pulses are then the incoherent sum of contributions from individual crystal points. Effect of timing jitter can be reduced by using thin crystals. Timing jitter in the SHG crystal can also be suppressed by strong focusing of the pumping beam. However, extreme focusing spoils the spatial mode structure and other properties of the generated beam. The sufficiently precise model of the timing jitter and its impact on the interference visibility can be created by the integration of the dip function $P(\Delta\tau)$ over the interaction length l in the nonlinear crystal with some weight function $h(x\mathcal{G})$. Here $\mathcal{G}$ is the GVM value for given material and frequencies. The resulting dip function $P_{\mathrm{J}}(\Delta\tau)$ can be written as,

$$P_{\mathrm{J}}(\Delta\tau) = \int_{-l/2}^{l/2} \mathrm{d}x h(x\mathcal{G}) P(\Delta\tau - x\mathcal{G}). \tag{2.32}$$

The effect of the timing jitter on the interference dip with Gaussian shape and the rectangular

weight function is illustrated at the Fig. 2.8. The rectangular shape of the weight function corresponds to the finite crystal length, along which the photons are generated with almost constant probability. The usable theoretical model of timing jitter can be found also in [31].
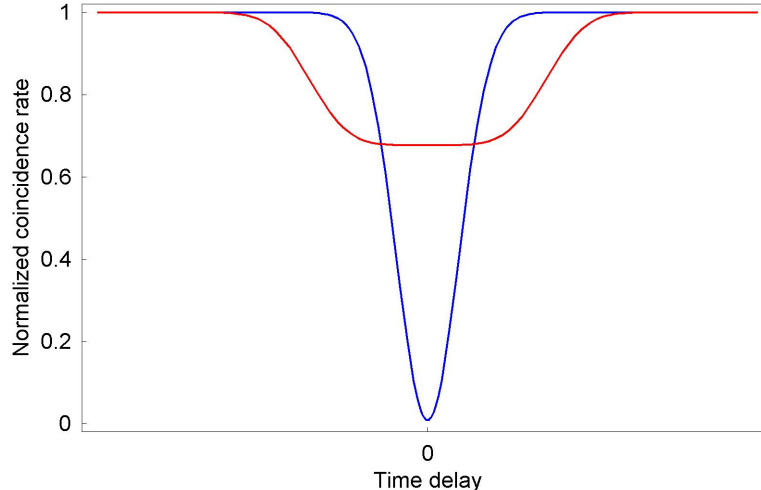

Figure 2.8: The illustration of the timing jitter effect on the interference dip with Gausian shape. The jitter is caused by the time uncertainty of the photon generation in the nonlinear processes due to GVM. The blue curve corresponds to the dip without jitter. The red curve represents the interference dip in the case of timing jitter with rectangular shape.

Most of the problems associated with the temporal and spectral mode matching can be overcome by extremely narrow spectral filtration that diminishes all the differences between the interacting pulses. However, in practice one should optimize the trade-off between filtering and count-rate of the developed source.

2.4.3 Polarization matching

The differences between polarization states of interacting photons can cause important contribution to their distinguishability and thus spoil the interference, especially in the fiber-based experiments where interference is implemented at the fiber-coupler. The polariazation state in the fiber is highly sensitive to fiber bending and gradients of the fiber temperature. The setting of particular polarization state at the given position in the fiber or at the fiber beam splitter is therefore not simple experimental task.

A generic polarization state $|\phi\rangle$ can be in the arbitrary basis described by two parameters. For the particular case of the HV basis with base-vectors $|H\rangle$ and $|V\rangle$ describing the horizontally and vertically polarized photons, respectively, the arbitrary state can be defined by the parameters α and β as

$$|\phi\rangle = \cos\frac{\alpha}{2}|H\rangle + \sin\frac{\alpha}{2}e^{i\beta}|V\rangle. \tag{2.33}$$

For given α and β the pure polarization state $|\phi\rangle$ can be represented by the point on the Poincare sphere, see Fig. 2.9. The points corresponding to mixed polarization states lie within the sphere. The parameter $\alpha \in \langle 0, \pi \rangle$ is represented by the parallels while the $\beta \in \langle 0, 2\pi \rangle$ is represented by the meridians and determines the deflection from the linear polarization. Overlap $\mathcal{O} = |\langle \phi_1 | \phi_2 \rangle|^2$ of any two polarization states thus varies periodically in dependence of the parameters α and β of both states.
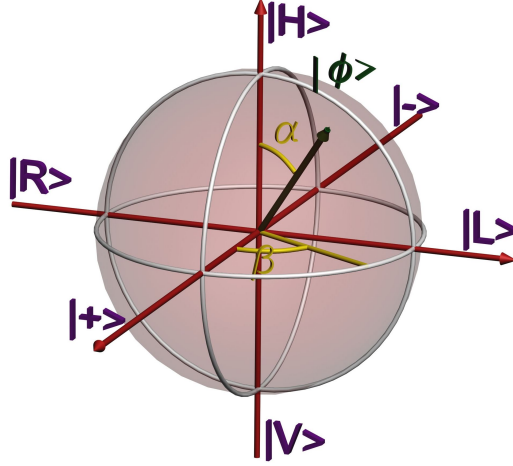

Figure 2.9: The useful graphical representation of polarization states—Poincare sphere. The linear polarizations $|H/V\rangle$ are at the poles while the linear diagonal $|+/-\rangle = 1/\sqrt{2}(|H\rangle \pm |V\rangle)$ and circular polarizations $|R/L\rangle = 1/\sqrt{2}(|H\rangle \pm i|V\rangle)$ are depicted at the equator.

The dependence of the Hong-Ou-Mandel type interference visibility V defined by (2.22) on the overlap $\mathcal{O}$ of the two interfering photons with general polarization states can be written as

$$V = \frac{\mathcal{O}}{2 - \mathcal{O}}. \tag{2.34}$$

The interference visibility varies from zero to one for the orthogonal and identical polarization states, respectively, and directly corresponds to the overlap of the interacted photons polarizations. The equation (2.34) holds for overlap $\mathcal{O}$ in any parameter of distinguishability of the interfering photons, i.e. also for the spatial, temporal and spectral mode overlaps.

Chapter 3

Experimental Realization of Three-Photon Source

The experimental realization of the two and especially three-photon source is a challenging task. Due to the complexity of the experimental scheme the individual parts of the setup will be described in separate sections.

3.1   Femtosecond laser

The initial near IR beam is obtained from Ti:sapphire femtosecond laser MIRA 900 (Coherent) pumped by diode-pumped solid-state laser Verdi V10 (Coherent) that emits light at 532 nm. Laser MIRA 900 is tunable from 700 to 980 nm and spectrum full width at half maximum (FWHM) can be adjusted approximately from 4 to 13 nm. In all experimental setups presented in this work the laser source MIRA 900 is working in pulsed regime with repetition rate of 76 MHz and central wavelength 800 nm. The beam from MIRA laser can reach average power up to 1 W and peak power of generated pulses up to 10^4 W. Manufacturer specifies that beam diameter at exit port of MIRA laser is (0.8 ± 0.2) mm and full angle beam divergence is (1.7 ± 0.3) mrad. Spatial mode of output beam has to be $\mathrm{TEM_{00}}$ and typical M^2 value is 1.1. Because of manufacturing tolerances in used optical components and ambient conditions affecting the laser cavity it is necessary to verify the specifications by measurement.

Measured waist radius is (0.280 ± 0.001) mm in horizontal direction and (0.372 ± 0.001) mm in vertical direction. The beam waist position is (26.9 ± 0.6) cm for horizontal direction and (19.5 ± 0.3) cm for vertical direction inside of MIRA laser measured from its front cover. Measured values of beam waist radius correspond approximately with the beam radius (0.4 ± 0.1) mm at the exit port of MIRA laser specified by manufacturer. Standard deviations include only statistical effects and they do not include possible systematical deviation of used WM100 beam profiler (Thorlabs). Ellipticity of the beam is about 35%. Positions of beam waist in horizontal and vertical direction are slightly different that is indication of astigmatism of the

beam.

Fundamental beam coming from laser MIRA is used for pumping the nonlinear process of frequency doubling and its depleted part is eventually used for preparation of weak coherent beam.

3.2 Second harmonic generation

Second harmonic generation (SHG) is a nonlinear process of frequency doubling, where pump wave generates another one with twice in frequency. It is degenerate case of three-wave-mixing effect, where energy and momentum conservation laws are expressed by $\vec{k_g} = 2\vec{k_p}$ and $\omega_g = 2\omega_p$, where indexes p and g denotes pump and generated wave, respectively.

In presented experiments the SHG near-UV beam is generated by the experimental setup depicted at Fig. 3.1. The setup contains optical elements for aligning and focusing pumping laser beam, nonlinear crystal, optical elements for correction of output beam astigmatism and dichroic mirror for separation the SHG beam at wavelength of 400 nm from depleted fundamental beam at wavelength of 800 nm. During the measurements two $\beta\mathrm{BaB_2O_4}$ (BBO) crystals cut for type-I phase matching with thicknesses 2 mm and 6 mm have been tested. The thinner crystal showed to be more suitable mainly for the three-photon interference due to the lower timing jitter (see section 2.4.2) and better spatial quality at the expense of slightly lower output power.
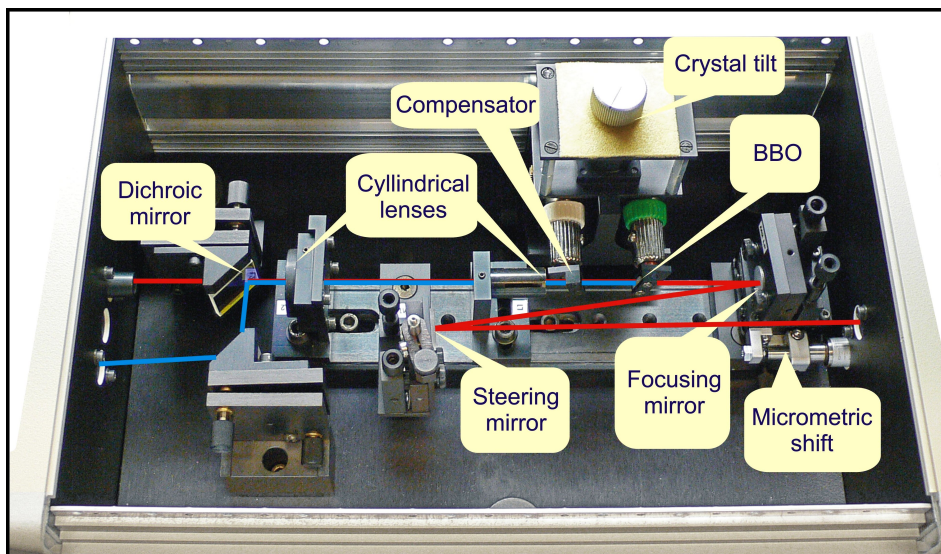

Figure 3.1: Experimental setup of second harmonic generation.

The near-UV SHG beam generated in 2 mm thick BBO crystal cut for type I phase matching has central wavelength of 400 nm and spectral width of approximately 1.2 nm. Beam diameter at crystal position is approximately $30\,\mu\mathrm{m}$. After astigmatism correction of the

SHG beam by two perpendicularly oriented cylindrical lenses with focal lengths of 50 mm and 150 mm the fundamental near IR and generated UV beam are separated by dichroic mirror. SHG output is adjusted for high power and spatial profile of the output beam as good as possible.

One of the most important characteristics of the SHG process is its conversion efficiency η. The measurement of conversion efficiency is based on comparing the average pumping power P_{in} and average converted power P_{out}. SHG conversion efficiency η depends on input power in nonlinear way [32],

$$\eta = \frac{P_{\mathrm{out}}}{P_{\mathrm{in}}} = \eta_{\mathrm{T}}[\tanh(\sqrt{2}\,g\,L\,\sqrt{P_{\mathrm{in}}})]^2. \tag{3.1}$$

Here η_{T} denotes linear transmissivity of passive optical elements utilized in process of SHG, g represents non-linear interaction constant, and L denotes length of the nonlinear crystal. Interaction constant g, which characterizes quality of SHG conversion, can be computed from conversion efficiency η measured for various pumping powers P_{in}. However, interaction constant is useful only if spatial and temporal properties of pumping beam remains unchanged. Interaction constant g allows to predict the SHG conversion efficiency η for any input P_{in} powers. The pump beam as well as output SHG beam powers are measured 120 times in 0.5 second intervals. Values of powers are acquired by power meter Fieldmaster GS (Coherent) with thermal detection head LM-1 (Coherent). The guaranteed accuracy of LM-1 head is $\pm5\%$. Since the time response of used power detector is very slow the fluctuations at short-time scale are not measurable. Measured values of input power and SHG conversion efficiency are fitted by computed theoretical curve by least-square method. Interaction constant g and transmissivity η_{T} are computed from parameters of fitted function. For our particular setup the interaction constant reaches $g = 629.3\,W^{-1/2} \cdot m^{-1}$ and the transmissivity is $\eta_{\mathrm{T}} = 0.471$.

3.3 Spatial filtering of frequency doubled beam

The mentioned spatial filtering methods are applied to complex multimode UV beam generated by nonlinear process of frequency up-conversion (SHG) in pulsed regime. The UV beam is spatially filtered either by the SM fiber or by 4-f system and its position and diameter at spatial filter entrance are set by a system of steering mirrors and lens L_{p}.

Experimental setup of spatial filtering by 30 cm SM bare (unconnectorized) fiber S405 (Thorlabs) is shown in Fig. 3.3 (a). The UV beam is focused at the fiber front-face by single aspheric lens with focal length of 15 mm. Small mode field area of step-index SM fiber for given wavelength together with poor spatial profile and considerable abberations of the SHG UV beam spoil the spatial filtering. Despite of mentioned difficulties the filtering efficiency of $\eta = (25 - 30)\,\%$ has been measured. The efficiency depends on spatial structure of the UV beam and thus on alignment of the SHG process. For the fundamental beam the same coupling method gives filtering efficiency $\eta_{\mathrm{max}} \approx 85\,\%$. The inefficiency is caused by power
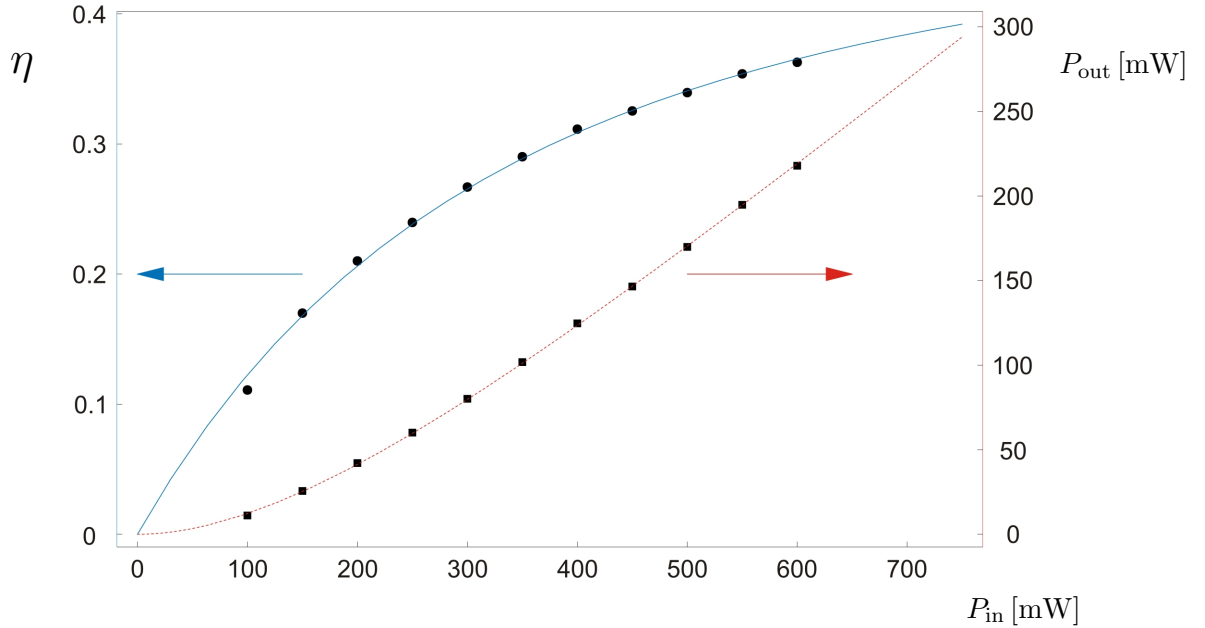
Figure 3.2: The measured values of conversion efficiency η (circles) and output power (squares) as a functions of input power P_{in}. Solid blue curve represents the theoretical model of conversion efficiency based on tanh-function and dashed red curve represents output average power. Parameters of the conversion efficiency function are fitted by means of least-square method. The absolute accuracy of the measurement is within $\pm 5\%$, see text for details.

losses of optical components (reflection, scattering, losses at aperture of coupling lens) and by reflection at the fiber end faces, as was discussed in previous section. After correcting on these inefficiencies the overlap of the UV beam with Gaussian mode reads $\eta_{\text{ovrl}} = (29-35)\,\%$.

The spatial profile of the UV beam is significantly improved after the SM fiber, however, its temporal and frequency properties are in general distorted by dispersion and nonlinear processes in the fiber. Material dispersion of S405 fiber is $-1150\,\text{ps/nm·km}$ at wavelength of $400\,\text{nm}$. Nonlinear effects, principally third order Kerr nonlinearity, begin to affect coupled beam due to high peak power density in core of SM fiber [33]. Wavelength spectrum broadening and rippling has been observed for increasing optical power transmitted by the fiber, see Fig. 3.4.

The measured spectrum widths (RMS) can be fitted by linear function that indicates the spectrum broadening is caused by Kerr self-phase modulation in the fiber, see Fig. 3.5 (left curve). Results are in good agreement with theoretical prediction [34] for spectral broadening of Gaussian pulse profile. Maximum used input average power reaches $100\,\text{mW}$ (peak power of $20\,\text{kW}$). For higher powers the fiber front face is damaged, probably due to ablation of fused silica by femtosecond pulses [35, 36]. For FC connectorized fiber the damage threshold is much lower, about $10\,\text{mW}$, due to the thermal load of fiber connector.

Photonic fibers made from undopped silica or even hollow-core fibers should eliminate

undesirable nonlinear effects due to the larger mode field diameter (MFD) than conventional step-index fibers. In particular case of full-core photonic fiber ESM-12-01 (endlessly single-mode, Crystal Fibre), its MFD is approximately $2\times$ larger than MFD of standard full-core fibers at the wavelength of 400 nm. Measurement with 40 cm bare photonic fiber results in the approximately same filtering efficiency as with the used full core fiber S405, while the observed spectrum broadening is less pronounced, see Fig. 3.5 (right curve). However, at higher input powers even these relatively small nonlinear effects could be obstructing for many applications. Dispersion of used ESM fiber is approximately -1100 ps/nm·km at wavelength of 400 nm [37] and the damage threshold of bare core ESM fiber is estimated to be the same as for the step-index S405 fiber.

The spectrum broadening and relatively low damage threshold can be overcome by a different method of spatial filtering, the 4-f system. SHG beam is transformed by two lenses $L_1 = 20$ cm and $L_2 = 12.5$ cm with the $50 \,\mu$m pinhole P50C (Thorlabs) in between, see Fig. 3.7 (b). Distances between L_1 lens and pinhole and between pinhole and L_2 lens are 24 cm
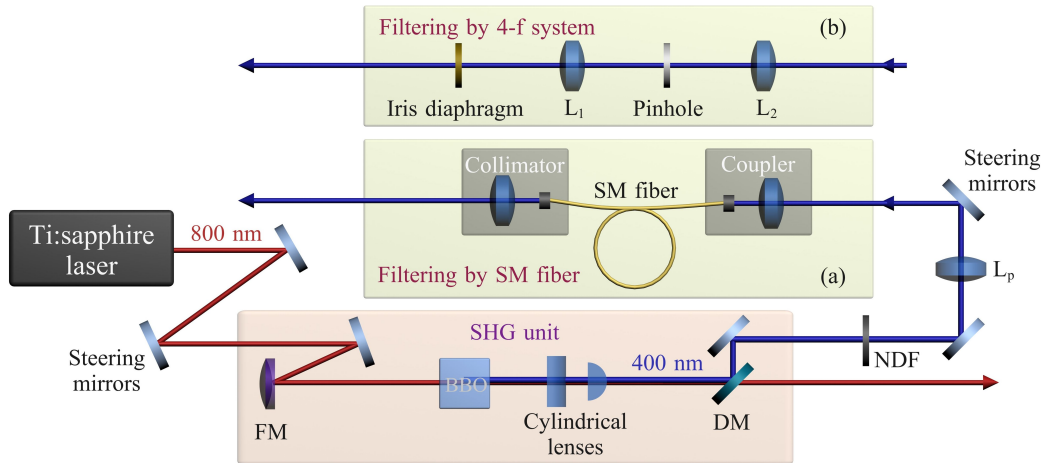

Figure 3.3: Scheme of SHG beam generation and spatial filtering. Femtosecond pulses from Ti:sapphire laser are used for pumping the nonlinear process of SHG. The fundamental near IR beam is focused by the focusing mirror (FM) with the focal length of 5 cm at the nonlinear crystal BBO. After correcting the astigmatism by two mutually perpendicular cylindrical lenses the UV the fundamental beam are separated by the dichroic mirror (DM). The UV beam power is adjusted by neutral density filter (NDF) and transformed by a system of steering mirrors and lens L_p. The spatial filtering is performed either by single mode (SM) fiber (a) or by 4-f system (b). In former case, the UV beam is further focused by aspheric coupling lens on fiber front-face and after spatial filtering by the SM fiber it is collimated to free space by a collimator. In the latter case, the UV beam is focused by lens L_1 at the gold-plated $50 \,\mu$m pinhole and collimated by lens L_2. Side maxima of diffraction pattern are removed by iris diaphragm, see text for details.

and 15 cm, respectively. Gold-plated pinhole is resistant to incident laser beams of relatively high power. Measured beam diameter at pinhole position is $220 \pm 20\,\mu$m and thus it is approximately $4\times$ larger than the pinhole diameter. Unwanted side maxima coming from diffraction of the beam at the pinhole are removed by iris diaphragm behind the collimation
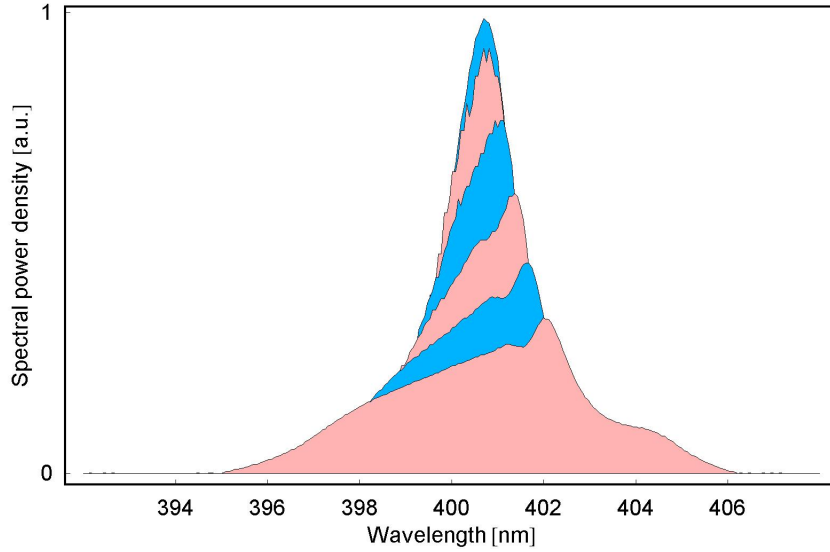

Figure 3.4: Observed spectrum broadening of filtered beam in S405 fiber caused principally by self-phase modulation. Graphs are plotted for increased average output powers (0.5, 1, 2, 4, 8, 16) mW from up to down. Broadening is more evident for higher transmitted powers.
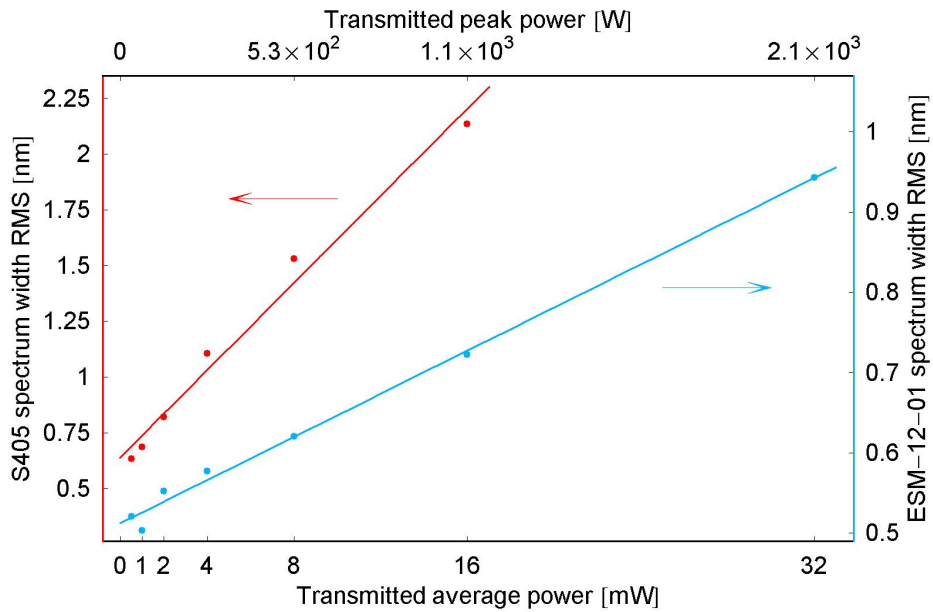

Figure 3.5: Measured spectrum RMS widths for both used fibers fitted by linear functions of transmitted optical power.

lens L_2. Filtering efficiency of the 4-f system reaches $\eta \approx 24\,\%$ and the measured overlap of filtered beam with Gaussian beam profile reads $\eta_{\mathrm{ovrl}} \approx 90\,\%$. The overlap is measured by coupling the filtered beam into the single mode fiber. Filtering efficiency and stability of the 4-f filtering system has been tested for SHG beam of average power up to $340\,\mathrm{mW}$. Due to the high overlap of output filtered beam with Gaussian profile and absence of nonlinear effects, the 4-f system seems to be the optimal filtering method of SHG femtosecond beam.

Up to now the total SHG power conversion efficiency and efficiency of spatial filtering have been discussed separately. However, only the power in well defined spatial mode is important. The total SHG power can be maximized for many possible alignments of SHG setup, while the spatial quality of SHG beam is out of control. Thus as a result, the high SHG conversion efficiency is obtained but, unfortunately, with low power in spatial mode we are interested in. The cases of high or low quality beam can be distinguished by spatial filter described above. Alternatively, the SHG setup can be adjusted directly for maximum power after spatial filter that yields the product of conversion efficiency and filtering efficiency as high as possible. The stable and rigid construction of spatial filter, particularly in the case of 4-f system, assures almost the constant properties of output spatial mode. In this way, the direction, width, optical power and almost single-mode spatial structure of the output beam have been maintained for months with uncertainty below $1\,\%$ despite of readjustment the SHG setup or even fundamental Ti:sapphire laser on daily basis.

3.4   Spontaneous parametric down conversion

The spatially well defined SHG beam is used for pumping the spontaneous parametric process of frequency down conversion (SPDC), see Fig. 3.7. SHG beam passes a $\lambda/2$ and $\lambda/4$ wave-plates by which the polarization of pumping beam is precisely adjusted to vertical. The SHG beam is focused at betabarium borate (BBO) crystal to the beam waist diameter of $450\,\mu\mathrm{m}$ in order to collect emitted photons efficiently [38]. The $2\,\mathrm{mm}$ thick BBO crystal is cut for type I phase matching. Generated pairs of degenerate photons at wavelength of $800\,\mathrm{nm}$ are emitted into a cone of half-opening angle 4 degrees. To tune precisely this angle the crystal is properly tilted in vertical direction.

Emitted pairs of photons are directed by the pair of steering mirrors in each SPDC arm to the fiber couplers, see Fig. 3.6. Photon pairs are filtered by interference filers (IF) with FWHM of $1.85\,\mathrm{nm}$ and $1.86\,\mathrm{nm}$ in signal (S) and idler (I) arms, respectively, as well as by cut-off filters which well block the crystal fluorescence at wavelengths in visible spectral range where the employed narrow interference filters have considerable transmissivity. Both the filters are centered at wavelength of $800.2\,\mathrm{nm}$ with peak transmissivity of $57.5\,\%$. For the precise matching of the filter central wavelength the fundamental laser beam wavelength is set for the maximal transmissivity of the used interference filters. The frequency filtered photon pairs are coupled into single-mode fibers which assure their perfect spatial indistinguishability.

The fiber coupling technique is described in [29]. Photons in (S) arm are guided by the single-mode fibers directly to the photodetector. The idler photons pass air gap which is used for the precision setting of the time delay between interfering photons. The one of two fiber-couplers in the air gap is mounted on the motorized linear stage MFA-CC with driver SMC100CC (Newport). The motorized stage has the shift range of $2.5\,\mathrm{cm}$ and repeatability of the position setting to within $2\,\mu\mathrm{m}$. The motorized stage is connected through the serial port to PC and is comfortably programmed that is suitable especially for the searching and scanning the Hong-Ou-Mandel dip where the automatization is necessary in order to measure large statistic ensemble for tens or even hundreds of length differences between interfered arms, i.e. hundreds shift position values. The air gap is adjusted for the approximately same coupling efficiency of $75\,\%$ at the whole shift range that confirms the beam is almost perfectly collinear with the direction of the shift. The average photon detection rates at the signal and idler detectors are $N_s = 11.5 \cdot 10^3$ counts/s and $N_i = 10.5 \cdot 10^3$ counts/s, respectively. The rate of the coincidence events is $N_{\mathrm{coinc}} = 800$ coincidences per second, that gives a two-photon coupling efficiency $\eta = 7.3\%$, see equation (2.4). The reached η is in good agreement with the losses of the signal and idler arms, which are given mainly by the transmissivity of the bandwidth filters, coupling losses, and detection efficiencies.

3.5 Preparation of third photon

The depleted fundamental (F) beam is properly separated from the frequency doubled UV beam by dichroic mirror and dispersion prism, see Fig. 3.8. The F beam pass the neutral density filter with optical density $\mathrm{OD} = 3$ that corresponds to the transmissivity $1/1000$. This attenuation is necessary particularly for blocking the reflection from fiber front-face coming
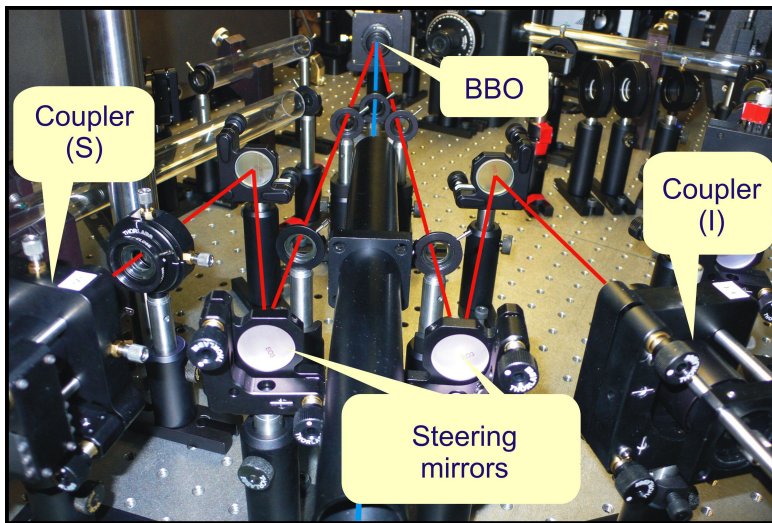

Figure 3.6: Photo of the SPDC setup geometry.

back to the laser, but also due to the prevention of the fiber end-face damage and enhancement of mechanical fiber attenuator setting precision. The beam is guided by the pair of mirrors to the self-made corner reflector. Corner reflector is made from two perpendicularly fixed mirrors mounted in montages with steering screws by which their perpendicularity can by precisely adjusted. Corner reflector is attached to the motorized linear stage MFA-CC with driver SMC100CC (Newport), see previous section for parameters. The range is in the expense of the resolution extended by factor two, because the beam travels the way to and from mirrors. In the case of the perfectly perpendicularly adjusted corner reflector the reflected beam has in the horizontal plane the same direction as the incoming beam, that decrease the demands for the precision of the motorized shift axis collinearity with the incoming beam direction. The output beam is spectrally filtered and coupled to single mode fiber, which leads to the pair of the mechanical fiber variable attenuators (VA), working on the simple principle of impeding the light passing the miniature space between the two coupling lenses by inserting a screw. In most of the measurements the count-rate of F beam is set by the attenuators to the value of $2 \cdot 10^5$ counts/s. The fiber coming from the second attenuator is rolled to the polarization controller by the means of $\lambda/2$, $\lambda/4$ and $\lambda/2$ wave-plates, although this correspondence is practically often not very satisfactory.

3.6 Detection, counting and coincidence logic

The photons guided by single-mode fibers are after relevant settings of their parameters and possible interactions incident at the silicon avalanche photodiodes (APDs) working in Geiger mode (SPCM-AQR, PerkinElmer). Employed APDs have detection efficiencies of 54 %, 55 % and 67 % and measured darkcounts of 110 counts/s, 170 counts/s and 60 counts/s in signal (S), idler (I) and fundamental (F) modes, respectively. The detection of the one or more photons is signalized by generating the 35 ns long TTL pulse at the output.

In the measurement of count-rate from individual detectors, the output TTL pulses are simply converted to NIM pulses and counted by four-channel counter (model 974, Ortec). The counter output is connected through the serial port to the computer and processed.

The measurement of twofold coincidences is based on the measuring the time delay between two incoming pulses. The time delay is converted to voltage and compared with some reference value. The output pulses from single-photon detectors are transmitted by coaxial cables to counting and coincidence logic which in the case of two-photon experiment consist of TTL/NIM converter, time-to-amplitude converter (TAC model 566, Ortec), single-channel analyzer (SCA model 550A, Ortec), and the four-channel counter. In our case the repetition rate of pulses is 76 MHz. That means the time delay between the consequent pulses is 13 ns and therefore the detection events with the lower mutual delay are taken as the coincidences. We used the time window of 10 ns that corresponds to 2 Volts on the SCA. Chosen reference value is sufficiently lower than the period of laser pulses and longer than any kind of timing

jitter that can arise from the detection or coincidence logics.

In three-photon experiment the coincidence logic is replaced by the fast digital four channel oscilloscope (Lecroy, WavePro 7200) with bandwidth 1.5 GHz and 20 GSa/s. The methods based on the triggering the coincidences in the single channel analyzer or using the four channel analyzer are not suitable for localizing and counting the 3-fold coincidences due to long (35 ns) TTL pulses from the detectors these techniques could highly contribute to false 3-fold coincidence events. The outputs from the (S), (I), and (F) detectors are connected to the three input channels of the oscilloscope. The events where all pulses are overlapped with the amplitude higher than 2 V at the time interval longer than 30 ns represent the true coincidence events if we neglect the dark-counts of individual detectors for now. The TTL pulse for each of such threefold coincidence event is sent by the oscilloscope auxiliary output to the counter.

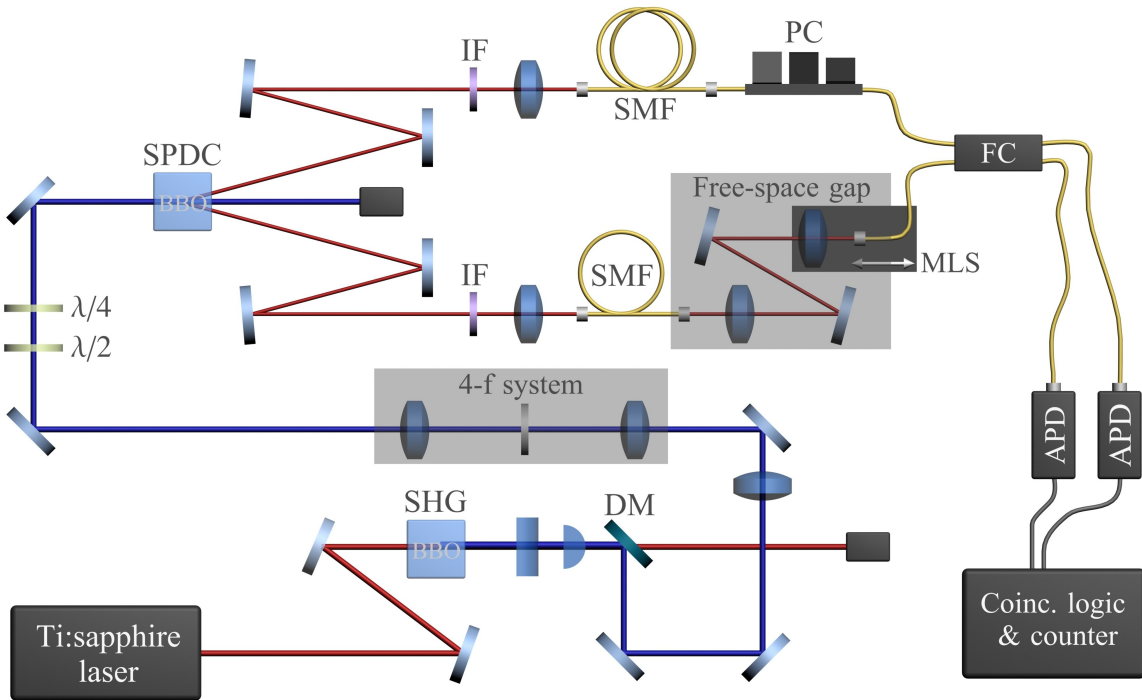## 3.7 Two-photon source and interference scheme

Figure 3.7: Two-photon source and interference setup.

The experimental scheme of two-photon source and Hong-Ou-Mandel interference is depicted at the Fig. 3.7. The fundamental femtosecond laser pulses are used for pumping the nonlinear process of second harmonic generation. Frequency doubled beam is after separation from the depleted fundamental beam spatially filtered. SHG beam pass the pair of waveplates

properly adjusted to set the perfect vertical polarization and is used for pumping the process of spontaneous parametric down conversion. Generated pairs are frequency filtered by bandwidth filters and coupled into single-mode fibers. Time delay between (S) and (I) photons is set by the length of air gap in the (I) arm at the scale of tens of femtoseconds. Signal and idler photons are then overlapped at the fiber-coupler (SIFAM, $R = 50.24\,\%, T = 49.76\,\%$, @800 nm). The fiber coupler output is guided to pair of single-photon detectors. Detectors output pulses are processed in coincidence logic and counter. Details of individual blocks can be found in previous sections.

3.8   Three-photon source and interference scheme

The scheme of the three-photon source and Rarity-Tapster type interference is depicted at the Fig. 3.8. The SHG and SPDC parts of the experiment are similar to these in two photon source, see previous section. The depleted fundamental beam is used for preparation of the weak coherent beam. SPDC generated photon pairs are used for generation of single photon states. The detection of idler photon triggers the signal photon. The single photon state in the (S) arm interferes at the balanced fiber coupler with the weak coherent state coming from the (F) arm. The signal coming from fiber coupler outputs is guided by single-mode fibers to the avalanche photodiodes. Pulses from all three detectors are processed in the fast oscilloscope and successful threefold coincidence events are triggered by the oscilloscope output and counted by counter. Typical threefold coincidence rate at the interference measurements has been 9 counts per 10 seconds, for the rate of the signal, idler and fundamental beam of 3600 counts/s, 8700 counts/s and 100 000 counts/sek, respectively. The photon rates in signal and fundamental modes are measured behind the beam splitter. For details about individual parts of the experiment see previous sections.
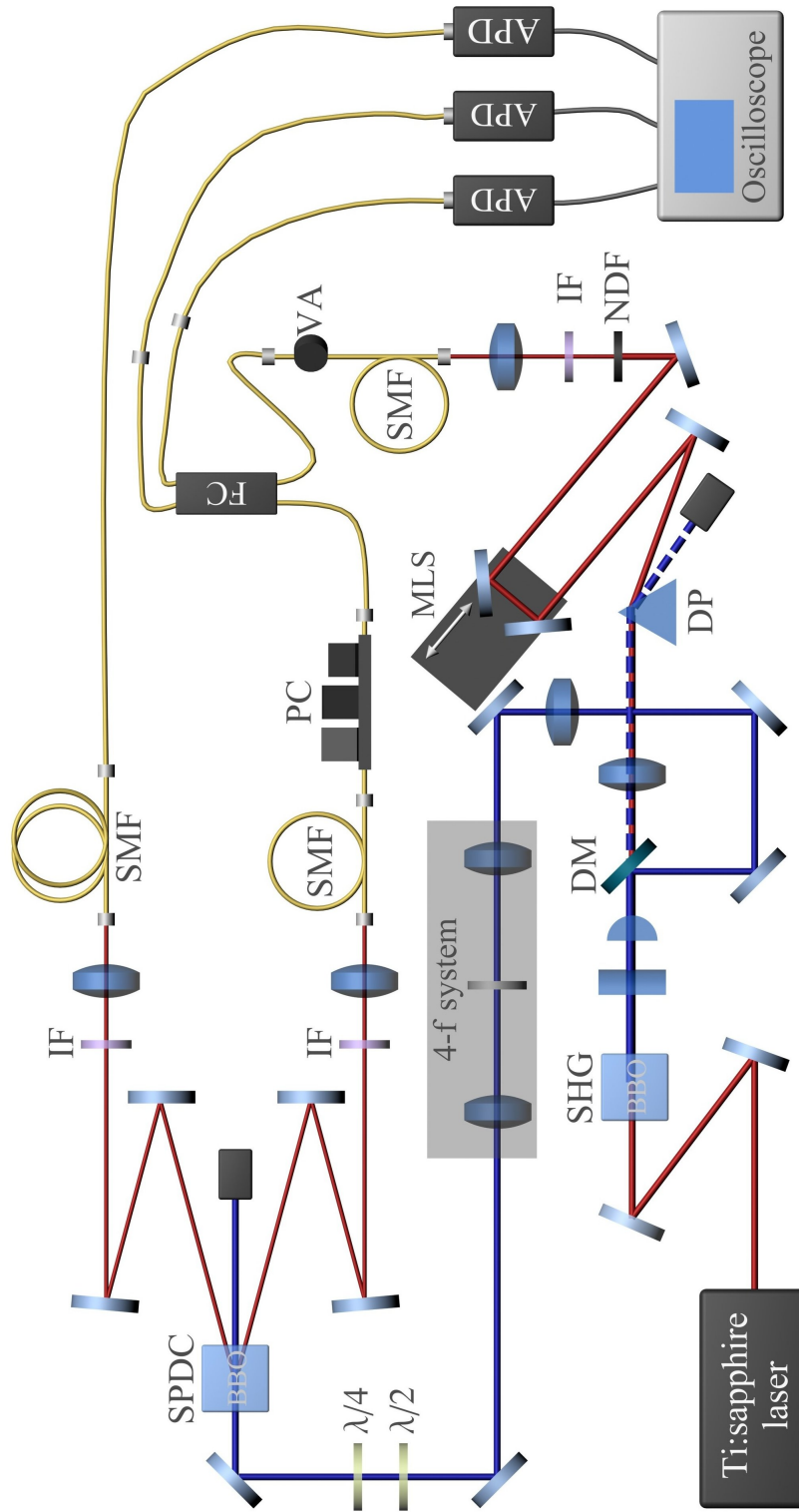
Figure 3.8: Three-photon source and interference setup.

Chapter 4

Measurement Results and Discussion

4.1 Two-photon interference

The perfect mutual indistinguishability of SPDC generated correlated photons is verified by the non-classical Hong-Ou-Mandel interference. In the ideal case, the two photons incident at two opposite input beam splitter ports leave always together in the one of the output ports and thus there is no possibility to observe the coincidence events between the detectors placed in the output beam splitter ports, see section 2.3.1.

The perfect coherence properties of our two photon source have been confirmed by the measured interference visibility extremely close to its limit. The highest measured visibility of HOM interference is 98.8 %, that is only 0.1 % below the calculated theoretical limit of 98.9 %, see Fig. 4.1. Repeatability of the measured HOM interference visibility over 98 % has been proved by numerous measurements. The measured HOM dip with the rich statistics can be seen at the Fig. 4.3.

The theoretical visibility is limited by false twofold coincidence detections. False coincidences are coming particularly from the events where two SPDC pairs are simultaneously generated. In contrast to CW pumped SPDC in the case of pumping by short pulses the probability of such events is due to the good time localization of pumping energy several orders of magnitude larger. For our coincidence rate the computed rate of such events is 0.84 coincidence per second, that gives the visibility limit of 98.9 %.

The two-photon dip full-width-at-half maximum (FWHM) in all measurements with 1.85 nm and 1.86 nm (FWHM) filters is $268\,\mu$m, that corresponds to dip temporal FWHM length in air of 895 fs. Using the (2.21) is evident, that dip time width is in perfect agreement with the computed Gaussian width of used filters. Since the shape of the used filters is far from perfect Gaussian, their measured shapes has been fitted by Gaussian curves, see Fig. 4.2. The Gaussian FWHM of the bandwidth filters are 2.03 nm and 2.04 nm that corresponds very well
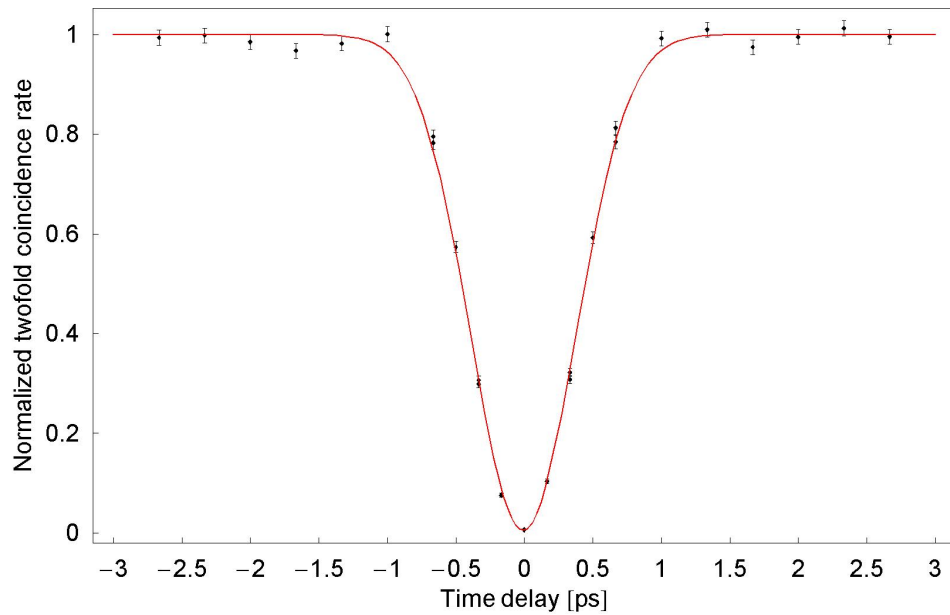
Figure 4.1: Two-photon HOM dip with visibility 98.8 % that is only 0.1 % below the theoretical limit. The errorbars correspond to one standard deviation and are computed by assuming the Poisson statistics of the coincidence events, i.e. the standard deviation equals to the square root of the expected value.
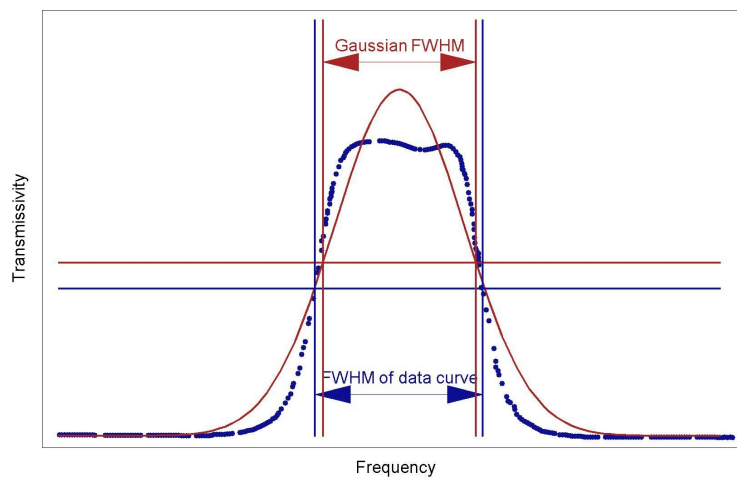

Figure 4.2: The fitted profile of the spectral filter shape and the corresponding Gaussian curve.

to filters FWHM of 2.1 nm computed from the measured dip. The negligible difference of 3% originates probably in the process of the filters shapes digitalization.
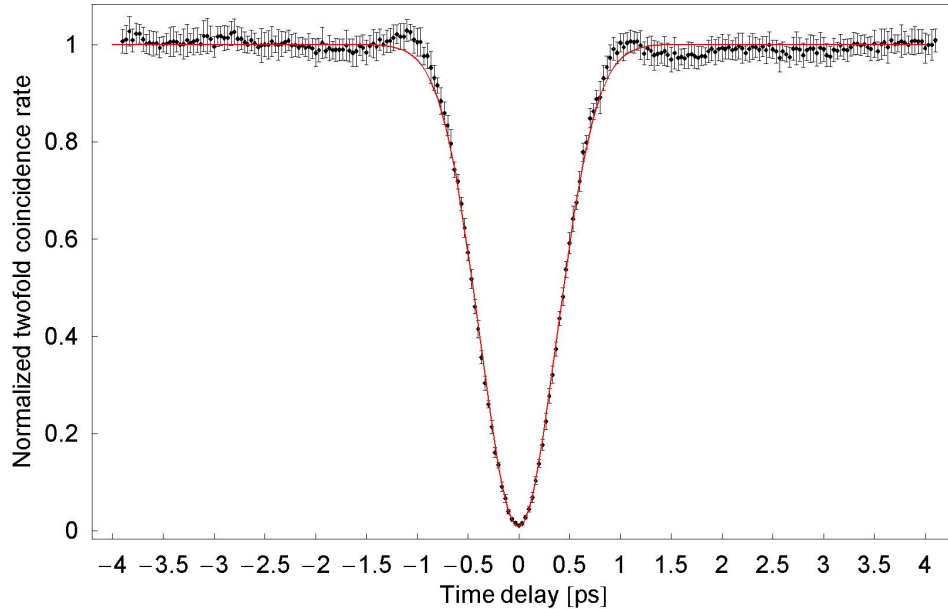
Figure 4.3: The two-photon HOM dip with visibility 98.1 %. The errorbars correspond to one standard deviation and are computed from the measured data.

4.2 Three-photon interference

If the weak coherent state cannot be distinguished from the one-photon state by any of its degree of distinguishability the probability of a coincident detections in the two output beam splitter ports goes to zero. A good approximation of a one-photon Fock state is provided by triggering of the single photons from SPDC emitted time-correlated photon pairs. Detection of one photon of the pair is used to herald the detection of its partner to within a time window given by the time duration of the pump pulse. An attenuated depleted fundamental beam is used as a weak coherent state. Since this beam has no phase correlation with the other beams coming from the SPDC, passes the different optical components, and undergoes different nonlinear processes the experiment can be thought as the interference between the independent sources [20].

The measurement of interference between the triggered single-photon states and attenuated coherent beam is visualized by the dip in the three-fold coincidence events as a function of the temporal delay between the photons interacting at the beam splitter. The visibility of the interference is very sensitive to parameters of all three employed photons, i.e. signal and idler photon from SPDC and 3rd photon from attenuated coherent beam. To assure the good indistinguishability of interacting photons is extra challenging particularly due to the difference of their paths. The various path lengths together with the different refraction indexes and dispersion coefficients of the interfered photons spoil the visibility interference due to the different pulse lengths and frequency chirps. The various processes change interacted
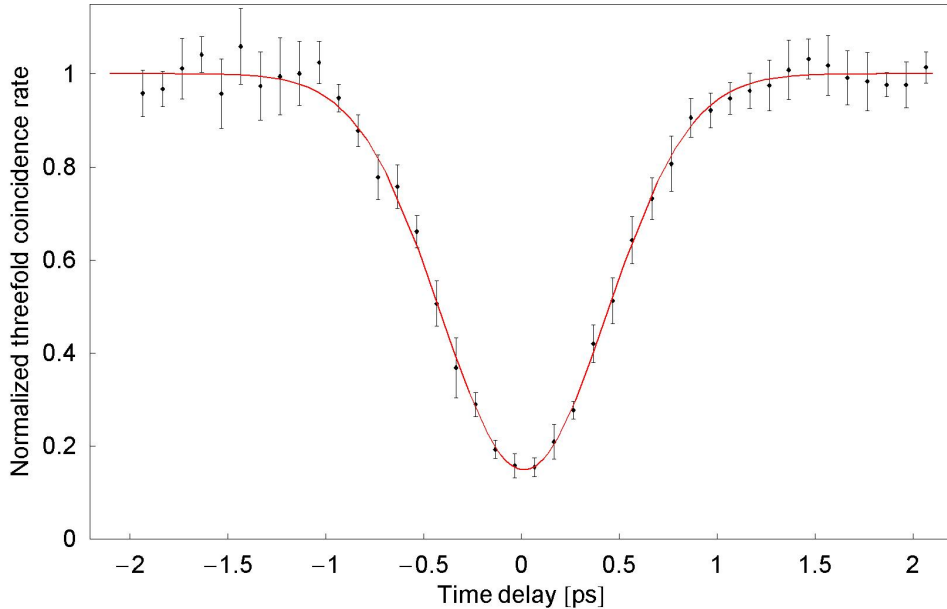
37

Figure 4.4: Three-photon Rarity-Tapster type interference. Triggered single-photon Fock state derived from SPDC is overlapped at the beam splitter with the attenuated coherent beam. By changing the optical path delay in the coherent state arm at the scale of picoseconds the dip in the the threefold coincidences with visibility of 74.1 % is measured. The threefold coincidence rate is 260 coincidences per 300 seconds.

photons temporal mode structures, spectral functions shapes and widths. Particularly the SHG process change the the temporal profile of the fundamental beam due to the quadratic dependence of the conversion efficiency on the peak pumping power. The both SHG and SPDC processes gives rise to the undesired timing jitter of the generated pairs due to the finite lengths of the employed nonlinear crystals.

In spite of the all mentioned obstacles in the reaching the photons indistinguishability we have demonstrated a three-photon interference with high visibility. The measured visibility of three-photon interference is 74.1 % with the time FWHM equal to 997 fs, see Fig. 4.4. The repeatability of the good properties of the source has been proved by several measurements with interference visibility over 72 %. The reached visibility is sufficiently greater than 50 %, that is clear evidence of non-classical three-photon interference. For 1.85 nm FWHM bandwidth filters the dip time width should equal to the width of the presented two-photon dip, see previous section. The 10 % spread of the dip width is caused especially by the timing jitter in the SHG and SPDC processes, i.e. the pulse length of the downconverted light is incoherently stretched by the walk-off effect due to the group velocity dispersion in the BBO crystals, see section 2.4.2.

The highest contribution to the interference imperfection is caused by the false threefold coincidences which are given particularly by events where two SPDC pairs are simultaneously

generated and from the two-photon contributions of the coherent state. The three-photon interference visibility is limited by the false coincidences to the value of 85 %. The another important loss of the interference visibility comes from the effect of the timing jitter. The GVM of the BBO crystals for the employed pulses frequencies is 180 fs/mm. The estimated interaction lengths of the SHG and SPDC crystals are 0.5 mm and 2 mm, respectively, what gives at least the 9 % loss of the visibility. The 1.5 % of the loss of visibility is in our case given by the imperfect matching of the spectral and temporal modes, see equation (2.27). The resulting computed interference visibility limit for our setup is 74.5 % which is in perfect correspondence with experimentally reached value.

The interference effect practically vanishes for the case where the SPDC signal photons are not triggered by their pair photons, see. Fig. 4.5. The low measured visibility of 2.3 % is consequence of high contribution of the two-photon states in the coherent state decomposition into Fock basis to the coincidences. This contribution is in the triggered experimental case several orders of magnitude lover.
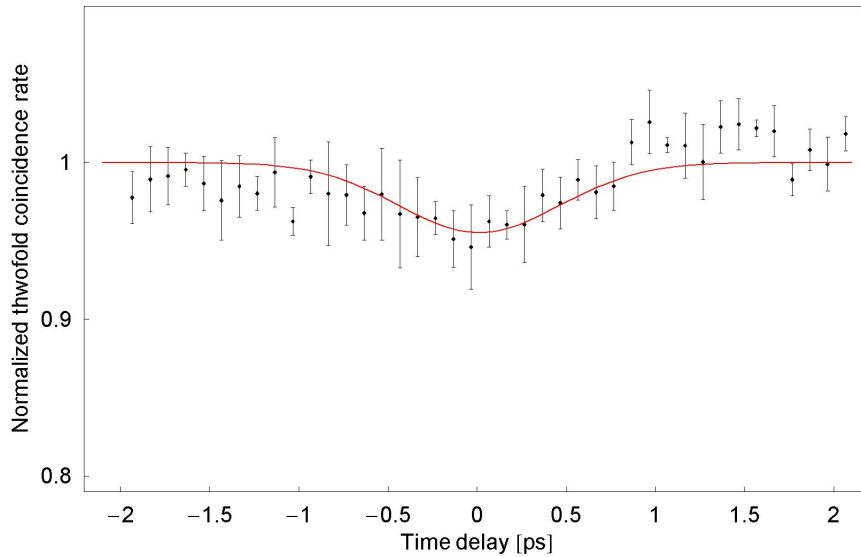

Figure 4.5: The untriggered version of Rarity-Tapster type interference. The attenuated coherent beam is overlapped with the SPDC photons. The dip in the twofold coincidence rate has the visibility of 2.3 %.

Chapter 5

Outlook

We now outline some new directions opened up by this work. The developed source of three correlated photons is almost ready for applications in the field of quantum information processing. Although the reached 3-photon source quality is very satisfactory, there are still possibilities to enhance the indistinguishability of generated photons. That can be achieved particularly by employing the thinner SPDC and SHG crystals, what should enhance the three-photon dip visibility for more than $5\,\%$, see section 2.4.2 for details. Further, the three-photon generation rate can be improved using the spectral filters with higher transmissivity and increasing the single-photon detectors efficiencies. The detector efficiency will be particularly slightly enhanced using the trap-detector scheme.

Parameters of the developed three-photon source can be efficiently verified by realization of some quantum information protocol, for example the teleportation of unknown polarization state [39]. Suppose that Alice and Bob share pairs of polarization-entangled particles. In order to teleport the polarization coded quantum bit $|\phi\rangle$ Alice performs the Bell-state measurement on her part of entangled pair and the photon to be teleported. After Alice measures one of the four Bell states, Bob's photon will be found in state $|\phi\rangle$ up to an unitary transformation. Alice informs Bob via classical communication channel about the measurement result and Bob performs the corresponding unitary operation. In our case the polarization entanglement can be prepared by mixing the two orthogonal states $|H\rangle$ and $|V\rangle$ at the beam splitter, what gives the singlet state $|\Psi^-\rangle = \frac{1}{\sqrt{2}}(|HV\rangle - |VH\rangle)$, see scheme of the experiment at Fig. 5.1. The modes 1 and 2 are mixed at the balanced beam splitter. Entangled pair is spread to two distant parties. With probability $\frac{1}{4}$ Alice projects the state of the teleported photon and photon from the entangled pair by measuring the coincidence between detectors 2 and 3 on the state $|\Psi^-\rangle$, the one of four Bell states. The Bob's particle is up to the irrelevant absolute phase shift in the state $|\phi\rangle$ that can be verified by the polarization analysis. The advantage of our realization could be an order of magnitude higher rate of the three-photon events than is usually reached in four-photon experiments. The theoretical prediction of teleportation fidelity $\mathcal{F}$ for the currently reached three-photon visibility $V = 74\,\%$ is $\mathcal{F} = \frac{1+V}{2} = 87\,\%$ that
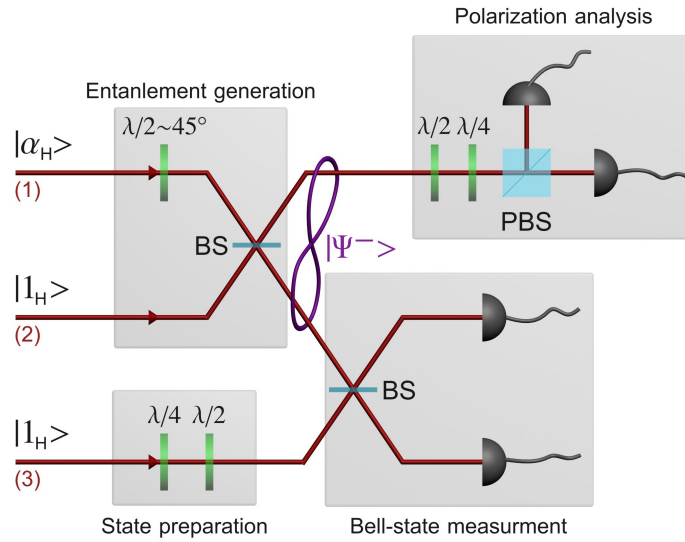
Figure 5.1: Teleportation scheme based on developed three-photon source.

is fully comparable to fidelities reached by other groups. However, after improving the source parameters, especially the timing jitter by changing SPDC crystal, the possible fidelity can be higher than 95 %.

Chapter 6

Conclusion

In the presented work the three-photon source based on the spontaneous parametric down-conversion and attenuated coherent beam has been designed and experimentally realized from scratch. The ultraviolet (UV) beam generated in the process of second harmonic generation (SHG) in pulsed femtosecond regime has been spatially filtered by spatial Fourier filtering by means of 4-f system. The spatially filtered UV beam has been used for pumping the nonlinear process of spontaneous parametric down conversion (SPDC). The spectrally and spatially filtered SPDC photons almost perfectly interfere at the balanced beam splitter. Two-photon Hong-Ou-Mandel interference with the raw visibility of 98.8 % has been measured which is only 0.1 % under the theoretical limit. The coherence time corresponds accurately to the bandwidth of employed narrow interference filters.

For the three-photon source the third photon mode has been obtained from attenuated fundamental laser beam depleted in the process of SHG. The good indistinguishability of the generated photons has been proved by the interference between attenuated coherent beam and single-photon state. The interference visibility of 74 % corresponds very well with theoretical limit computed for our particular experimental scheme. The highest contributions to the interference imperfection are false threefold coincidences and effect of the timing jitter due to the group velocity mismatch in nonlinear crystals of finite width. The suggestions for the three-photon interference visibility enhancement as well as the intended applications of the realized source has been proposed in previous chapter. The coincidence rate of about one threefold coincidence event per second has been observed which is fully comparable with the sources used recently to demonstrate the interference between independent sources [20] and to demonstrate a quantum circuit using linear optics gates [23].

The reached threefold coincidence rate together with precise definition of modes, indistinguishability of generated photons, and proper timing enable a great number of notable experiments involving the interference of generated photons from the field of quantum information processing.

Bibliography

[1] P. W. Shor, Polynomial-Time Algorithms for Prime Factorization and Discrete Logarithms on a Quantum Computer, SIAM J. Sci. Statist. Comput. **26**, 1484 (1997).

[2] L. K. Grover, Quantum Mechanics Helps in Searching for a Needle in a Haystack, Phys. Rev. Lett. **79**, 325 (1997).

[3] C. Y. Lu, D. E. Browne, T. Yang, and J. W. Pan,Demonstration of a Compiled Version of Shors Quantum Factoring Algorithm Using Photonic Qubits, Phys. Rev. Lett. **99**, 250504 (2007)

[4] L. M. K. Vandersypen, M. Steffen, G. Breyta, C. S. Yannoni, M. H. Sherwood, and I. L. Chuang, Experimental realization of Shors quantum factoring algorithm using nuclear magnetic resonance, Nature (London) **414**, 883 (2001).

[5] L. M. K. Vandersypen, M. Steffen, M. H. Sherwood, C. S. Yannoni, G. Breyta, and I. L. Chuang, Implementation of a three-quantum-bit search algorithm, Appl. Phys. Lett. **76**, 646 (2000)

[6] D. Bouwmeester, J. W. Pan, K. Mattle, M. Eibl, H. Weinfurter, and A. Zeilinger, Experimental quantum teleportation, Nature (London) **390**, 575 (1997).

[7] J. W. Pan, D. Bouwmeester, H. Weinfurter, and A. Zeilinger, Experimental entanglement swapping: Entangling photons that never interacted, Phys. Rev. Lett. **80**, 3891 (1998).

[8] J. W. Pan, S. Gasparoni, R. Ursin, G. Weihs, and A. Zeilinger, Experimental entanglement purification of arbitrary unknown states, Nature (London) **22**, 423 (2003)

[9] L. Mandel and E. Wolf, *Optical Coherence and Quantum Optics* (Cambridge University Press, Cambridge, 1995).

[10] S. Castelletto, I. P. Degiovanni, A. Migdall, and M. Ware, On the measurement of two-photon single-mode coupling efficiency in parametric down-conversion photon sources, New J. Phys. **6**, 87 (2004).

[11] T. B. Pittman, B. C. Jacobs, and J.D. Franson, Heralding Single Photons from Pulsed Parametric Down-Conversion, Optics Communications **246**, 545 (2005).

[12] T. E. Keller and M. H. Rubin, Theory of two-photon entanglement for spontaneous parametric down-conversion driven by a narrow pump pulse, Phys. Rev. A **56**, 1534 (1997).

[13] M. H. Rubin, D. N. Klyshko, Y. H. Shih, and A. V. Sergienko, Theory of two-photon entanglement in type-II optical down-conversion, Phys. Rev. A **50**, 5122 (1994).

[14] G. Di Giuseppe, L. Haiberger, and F. De martini, Quantum interference and indistinguishability with femtosecond pulses, Phys. Rev. A 56, R21 (1997).

[15] E. Knill, R. Laflamme, and G. J. Milburn, A scheme for efficient quantum computation with linear optics, Nature (London) **409**, 46 (2001).

[16] C. K. Hong, Z. Y. Ou, and L. Mandel, Measurement of subpicosecond time intervals between two photons by interference, Phys. Rev. Lett. **59**, 2044 (1987).

[17] P. Kok, W. J. Munro, K. Nemoto, T. C. Ralph, J. P. Dowling, and G. J. Milburn, Linear optical quantum computing, Rev. Mod. Phys. **79**, 135, (2007).

[18] T. Nagata, R. Okamoto, J. L. O'Brien, K. Sasaki, and S. Takeuchi, Beating the Standard Quantum Limit with Four-Entangled Photons, Science **316**, 726 (2007).

[19] J. Perina, *Quantum Statistics of Linear and Nonlinear Optical Phenomena* 2nd completely rev. ed., (Informatorium, Prague, 1991).

[20] J. G. Rarity, P. R. Tapster, and R. Loudon, Non-classical interference between independent sources, J. Opt. B: Quantum Semiclass. Opt. **7**, S171 (2005).

[21] T. B. Pittman, B. C. Jacobs, and J.D. Franson, Probabilistic Quantum Encoder for Single-Photon Qubits, Phys. Rev. A **69**, 042306 (2004).

[22] T. B. Pittman and J.D. Franson, Violation of Bells Inequality with Photons from Independent Sources, Phys. Rev. Lett. **90**, 240401 (2003).

[23] T. B. Pittman, B. C. Jacobs, and J. D. Franson, Experimental demonstration of a quantum circuit using linear optics gates, Phys. Rev. A **71**, 032307 (2005).

[24] T.B. Pittman, M. J. Fitch, B. C Jacobs, and J. D. Franson, Experimental Controlled-NOT Logic Gate for Single Photons in the Coincidence Basis Phys. Rev. A **68**, 032316 (2003).

[25] C. H. Monken, P. H. Souto Ribeiro, and S. Pádua Transfer of angular spectrum and image formation in spontaneous parametric down-conversion, Phys. Rev. A **57**, 3123 (1998).

[26] S. P. Walborn, A. N. de Oliveira, S. Pádua, and C. H. Monken, Multimode Hong-Ou-Mandel Interference, Phys. Rev. Lett. **90**, 143601 (2003).

[27] G. Molina-Terriza, S. Minardi, Y. Deyanova, C. I. Osorio, M. Hendrych, and J. P. Torres, Control of the shape of the spatial mode function of photons generated in noncollinear spontaneous parametric down-conversion, Phys. Rev. A **72**, 065802 (2005).

[28] O. Wallner and W. R. Leeb, Minimum length of a single-mode fiber spatial filter, J. Opt. Soc. Am. A **19**, 2445 (2002).

[29] L. Slodička, Realization of spatial modes filtration by single-mode optical fiber, bachelor thesis, Faculty of Natural Sciences, Palacký University (2006).
http://optics.upol.cz/download/studenti_archiv_praci/2006/Slodicka_L_Bc_2006.pdf

[30] Z. Y. Ou, Multi-Photon Interference and Temporal Distinguishability of Photons, Phys. Rev. A **74**, 063808 (2006).

[31] R. Kaltenbaek, Entanglement swapping and quantum interference with independent sources, dissertation thesis, Fakulty of Physics, University of Vienna (2007)

[32] B. E. A. Saleh and M. C. Teich, *Fundamentals of Photonics* (John Wiley & Sons, Inc., 1994).

[33] S. A. Akhmanov, V. A. Vysloukh, and A. S. Chirkin, *Optics of femtosecond lasers* (American Institute of Physics, 1992).

[34] R. A. Fisher and W. K. Bishel, Numerical studies of the interplay between self-phase modulation and dispersion for intense plane-wave laser pulses, J. Appl. Physics **46**, 4921 (1975).

[35] M. Lenzner, J. Kruger, S. Sartania, Z. Cheng, Ch. Spielmann, G. Mourou, W. Kautek, and F. Krausz, Femtosecond optical breakdown in dielectrics, Phys. Rev. Lett. **80**, 4076 (1998).

[36] A. Ch. Tien, S. Backus, H. Kapteyn, M. Murnane, and G. Mourou, Short-pulse laser damage in transparent materials as a function of pulse duration, Phys. Rev. Lett. **82**, 3883 (1999).

[37] H. P. Uranus, Guiding light by and beyond the total internal reflection mechanism, dissertation thesis, MESA+, University of Twente (2005).

[38] A. Ling, Anta Lamas-Linares, and C. Kurtsiefer, Absolute emission rates of Spontaneous Parametric Down Conversion into single transverse Gaussian modes, arXiv:0801.2220v1

[39] C. H. Bennet, G. Brassard, C. Crpeau, R. Jozsa, A. Peres, and W. K. Wootters, Teleporting an unknown quantum state via dual classical and Eistein-Podolsky-Rosen channels, Phys. Rev. Lett. **70**, 2011 (1993).